Effect of intermodular connection on fast sparse synchronization in clustered small-world neural networks

Sang-Yoon Kim* and Woochang Lim†

Institute for Computational Neuroscience and Department of Science Education, Daegu National University of Education, Daegu 705-115, Korea

(Received 13 July 2015; revised manuscript received 22 September 2015; published 23 November 2015)

We consider a clustered network with small-world subnetworks of inhibitory fast spiking interneurons and investigate the effect of intermodular connection on the emergence of fast sparsely synchronized rhythms by varying both the intermodular coupling strength J_{inter} and the average number of intermodular links per interneuron $M_{\text{syn}}^{(\text{inter})}$. In contrast to the case of nonclustered networks, two kinds of sparsely synchronized states such as modular and global synchronization are found. For the case of modular sparse synchronization, the population behavior reveals the modular structure, because the intramodular dynamics of subnetworks make some mismatching. On the other hand, in the case of global sparse synchronization, the population behavior is globally identical, independently of the cluster structure, because the intramodular dynamics of subnetworks make perfect matching. We introduce a realistic cross-correlation modularity measure, representing the matching degree between the instantaneous subpopulation spike rates of the subnetworks, and examine whether the sparse synchronization is global or modular. Depending on its magnitude, the intermodular coupling strength J_{inter} seems to play "dual" roles for the pacing between spikes in each subnetwork. For large J_{inter}, due to strong inhibition it plays a destructive role to "spoil" the pacing between spikes, while for small J_{inter} it plays a constructive role to "favor" the pacing between spikes. Through competition between the constructive and the destructive roles of J_{inter}, there exists an intermediate optimal J_{inter} at which the pacing degree between spikes becomes maximal. In contrast, the average number of intermodular links per interneuron $M_{\text{syn}}^{(\text{inter})}$ seems to play a role just to favor the pacing between spikes. With increasing $M_{\text{syn}}^{(\text{inter})}$, the pacing degree between spikes increases monotonically thanks to the increase in the degree of effectiveness of global communication between spikes. Furthermore, we employ the realistic sub- and whole-population order parameters, based on the instantaneous sub- and whole-population spike rates, to determine the threshold values for the synchronization-unsynchronization transition in the sub- and whole populations, and the degrees of global and modular sparse synchronization are also measured in terms of the realistic sub- and whole-population statistical-mechanical spiking measures defined by considering both the occupation and the pacing degrees of spikes. It is expected that our results could have implications for the role of the brain plasticity in some functional behaviors associated with population synchronization.

DOI: 10.1103/PhysRevE.92.052716 PACS number(s): 87.19.lm, 87.19.lc

I. INTRODUCTION

Recently, much attention has been paid to brain rhythms in health and disease [1,2]. Particularly, we are interested in fast sparsely synchronized cortical rhythms which are associated with diverse cognitive functions such as sensory perception, feature integration, selective attention, and memory formation [3]. At the population level, local field potential recordings have been observed to show synchronous fast oscillations [e.g., γ rhythm (30–100 Hz) and ultrafast sharp-wave ripple (100–200 Hz)], while individual neuronal recordings have been found to exhibit stochastic and intermittent spike discharges [4–10]. Thus, single-cell firing activity differs markedly from the population oscillatory behavior. These sparsely synchronized rhythms are in contrast to fully synchronized rhythms. For the case of full synchronization, individual neurons fire regularly at the population frequency like the clock oscillators [11]. Hence, the fully synchronized oscillations may be well described by using the conventional coupled-oscillator model composed of suprathreshold spiking neurons above a threshold in the absence of noise or for weak noise [12]. However, such coupled-oscillator models are not adequate for describing sparse synchronization because individual neurons fire stochastically at low rates like Geiger counters. Brunel *et al.* in Refs. [13–18] developed a framework appropriate for description of fast sparse synchronization by taking an opposite view from that of coupled oscillators. Under the condition of strong external noise, suprathreshold spiking neurons discharge irregular firings as Geiger counters, and then the population state becomes unsynchronized. However, when inhibitory recurrent feedback becomes sufficiently strong, this asynchronous state may be destabilized, and then a synchronous population state with irregular and intermittent individual discharges emerges. For this case, average total (external excitatory plus recurrent inhibitory) input current into individual neurons is subthreshold, but stochastic and intermittent firings are triggered when fluctuations (due to noise in external and recurrent inputs) cross a threshold. In this way, under the balance between strong external noise and strong recurrent inhibition, fast sparse synchronization was found to occur in networks of suprathreshold neurons [13–18]. Similar sparsely synchronized rhythms were also found to appear via cooperation of noise-induced spikings of subthreshold neurons (which cannot fire spontaneously without noise) [19–21]. However, in contrast to the above works on suprathreshold neurons, sparse synchronization for the case

*sykim@icn.re.kr
†wclim@icn.re.kr

of subthreshold neurons has been found to appear under relatively weak external noise and recurrent inhibition, and the sparsely synchronized rhythms were also found to be slow when compared with the suprathreshold case.

In this paper, we are concerned about the emergence of fast sparsely synchronized rhythms in an ensemble of suprathreshold neurons, as in the previous works of Brunel *et al.* [13–18], where both random and global synaptic couplings were considered. However, connection architecture of the real brain has been found to have complex topology which is neither regular nor random [22–30]. Particularly, mammalian (e.g., cat and macaque) brain anatomical networks and human brain functional (fMRI) networks have been revealed to have a modular structure composed of relatively sparsely linked clusters with spatial localization, as in social, technological, and biological complex networks [31–38]. Within each cluster, nodes are highly interconnected and exhibit similar connectional and functional features. This clustered organization of the brain network reveals the anatomical substrate for segregation which refers to the subdivision of the brain into regions specialized in particular functional tasks [39–41]. This segregation allows the brain to process information in parallel, simultaneously by distinct populations of neurons. However, for emergence of a coherent perception and comprehensive understanding of the environment as a whole, specialized information of different modalities and features should be integrated. This integration refers to the capacity of a system to collect information of different nature and combine it to produce new useful information. For example, sensory perception requires the binding of the features of a receptive field (e.g., color, orientation, and position of a visual object). In this way, brain connectivity should be organized into a balance between segregation (specialization) and integration (binding) [42–46]. Here in our brain network we take into consideration the modular structure of the real brain. For modeling the modular structure of a real brain, we consider a clustered network composed of sparsely connected subnetworks. The subnetworks stand for the modules (clusters) of the brain. As is also known, the connection structure in each module of the real brain reveals complex topology such as small-worldness and scale-freeness [22–30]. Here each subnetwork (representing a cluster) is modeled as the Watts-Strogatz small-world network which interpolates between the regular lattice with high clustering (i.e., high cliquishness of a typical neighborhood) and the random graph with short path length (i.e., average short separation between two neurons represented by average number of synapses between two neurons along the minimal path) by varying the rewiring probability $p_{\rm rewiring}$ from local to long-range connections; $p_{\rm rewiring} = 0$ and 1 correspond to the regular lattice and the random graph, respectively [47–49]. The Watts-Strogatz model for the small-world subnetwork may be regarded as a cluster-friendly extension of the random network by reconciling the six degrees of separation (small-worldness) [50,51] with the circle of friends (clustering). Many recent works on various subjects of neurodynamics have been done in small-world networks with predominantly local connections and rare long-distance connections [52–63]. The effect of this small-world connectivity on fast sparse synchronization has also been studied in our recent work [64].

We note that real brain networks, consisting of sparsely interconnected modules, are far more complex than minimal nonmodular models such as small-world and scale-free networks. The main purpose of our study is to investigate the emergence of sparsely synchronized rhythms in more realistic modular networks. Clustered neural networks composed of regular, small-world, and scale-free subnetworks have been employed for study on several subjects of neurodynamics [39–41,65–69]. For our aim, we consider a clustered network with small-world subnetworks of inhibitory spiking neurons and investigate the effect of intermodular connection on emergence of fast sparsely synchronized rhythms. In the absence of intermodular coupling, we consider three cases for the intramodular dynamics in subnetworks: (1) synchronized in all identical subnetworks, (2) unsynchronized in all identical subnetworks, and (3) synchronized and/or unsynchronized in nonidentical subnetworks. For each case, we study the population states by changing both the intermodular coupling strength $J_{\rm inter}$ and the average number of intermodular links per interneuron $M_{\rm syn}^{\rm (inter)}$. Consequently, two kinds of sparse synchronization such as modular and global synchronization are found, in contrast to the case of nonmodular networks [13–18,64,70]. For the case of modular sparse synchronization, the population behavior reveals the modular structure; hence, the degree of sparse synchronization in the whole population becomes less than that in the subnetworks, because the intramodular dynamics of subnetworks make some mismatching. In contrast, for the case of global sparse synchronization, the population behavior is globally identical, independently of the cluster structure, because the intramodular dynamics of subnetworks make perfect matching. These modular and global synchronizations may be well visualized in the raster plots of spikes. For the case of synchronization, synchronous "stripes" (composed of spikes and indicating population synchronization) appear successively in the raster plots, while spikes are completely scattered (without forming any stripes) in the case of unsynchronization. Synchronization pacing (representing the smearing of spiking stripes: less smearing, better pacing) varies depending on $J_{\rm inter}$. For large $J_{\rm inter}$ it plays a destructive role to spoil the pacing between sparse spikes, because of strong inhibition. Hence, when passing a large threshold a transition to unsynchronization occurs. However, for small $J_{\rm inter}$ it plays a constructive role to favor the pacing between spikes in each subnetwork. Hence, via competition between the constructive and the destructive roles of $J_{\rm inter}$, there appears an intermediate optimal $J_{\rm inter}$ at which the pacing degree between spikes becomes maximal. In this way, $J_{\rm inter}$ plays dual roles for the pacing between spikes in each subnetwork, depending on its magnitude. On the other hand, the average number of intermodular links per interneuron $M_{\rm syn}^{\rm (inter)}$ plays a role just to favor the pacing between spikes. As $M_{\rm syn}^{\rm (inter)}$ is increased, the pacing degree between spikes increases monotonically due to the increase in the degree of effectiveness of global communication between spikes. To make characterization of the synchronization-unsynchronization transitions in the sub- and whole populations, we employ the realistic sub- and whole-population order parameters, based on the instantaneous sub- and whole-population spike rates [71]. Moreover, we introduce

a realistic cross-correlation modularity measure, representing the matching degree between the instantaneous subpopulation spike rates of subnetworks, and examine whether the sparse synchronization is global or modular. The degrees of modular and global sparse synchronization are also measured in terms of the realistic sub- and whole-population statistical-mechanical spiking measures defined by considering both the occupation and the pacing degrees of the spikes [71].

This paper is organized as follows. In Sec. II A, we describe a clustered network with small-world subnetworks of inhibitory fast spiking (FS) interneurons, and then the governing equations for the population dynamics are given. Detailed explanations on methods for the characterization of individual and population states in clustered networks are also given in Sec. III. Then, in Sec. IV we investigate the effect of intermodular connection on the emergence of fast sparsely synchronized rhythms by varying both J_{inter} and $M_{\text{syn}}^{(\text{inter})}$. Finally, a summary is given in Sec. V.

II. CLUSTERED SMALL-WORLD NETWORK OF INHIBITORY FS IZHIKEVICH INTERNEURONS

In this section, we first describe our cluster network composed of $M(=3)$ small-world subnetworks, each of which contains L FS Izhikevich interneurons in Sec. II A. Then the governing equations for the population dynamics in the clustered small-world network are given in the Sec. II B.

A. Clustered small-world networks

We consider a clustered network with M $(=3)$ small-world subnetworks. Each small-world subnetwork consists of L inhibitory interneurons equidistantly placed on a one-dimensional ring of radius $L/2\pi$. For illustrative purposes, an example of the clustered network topology is shown in Fig. 1. Each of the three subnetworks, consisting of $L = 20$ interneurons, is modeled as the Watts-Strogatz small-world network which interpolates between the regular lattice and the random graph by varying the rewiring probability p_{rewiring} from local to long-range connections [47–49]. We start from the case of $p_{\text{rewiring}} = 0$, corresponding to a directed regular ring lattice where each interneuron is coupled to its first $M_{\text{syn}}^{(\text{intra})}$ $(=4)$ neighbors ($M_{\text{syn}}^{(\text{intra})}/2$ on either side) via outward synapses. Then we rewire each outward connection at random with probability p_{rewiring} such that self-connections and duplicate connections are excluded, and the value of p_{rewiring} is 0.25 for the case of Fig. 1. Within each small-world subnetwork, the average number of intramodular synaptic inputs per interneuron is $M_{\text{syn}}^{(\text{intra})}$, while there exist eight sparse random intermodular links between small-world subnetworks.

B. Governing equations for the population dynamics

As an element in our clustered small-world network, we choose the FS Izhikevich interneuron model which is not only biologically plausible, but also computationally efficient [72–75]. We consider the clustered network composed of $M(=3)$ small-world subnetworks, each of which consisting of L FS interneurons; $L = 10^3$, except for the case of order parameters and spatial cross-correlation functions. The following Eqs. (1)–(7) govern the population dynamics in the clustered small-world network,

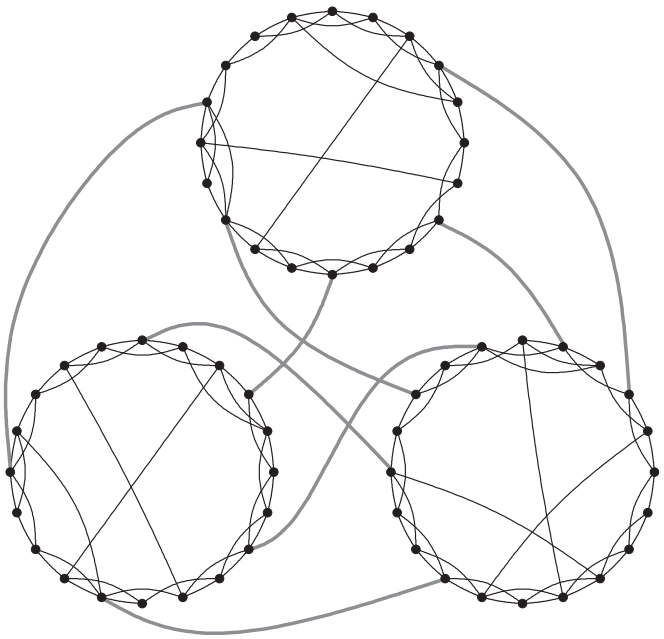

FIG. 1. Schematic representation of the clustered small-world network topology. The whole network consists of $M(=3)$ Watts-Strogatz small-world subnetworks, each of them containing $L(=20)$ interneurons. Within each subnetwork, the average number of intramodular synaptic inputs per interneuron is $M_{\text{syn}}^{(\text{intra})}(=4)$, while there are eight sparse random intermodular connections (denoted by heavy lines) between the subnetworks.

$$C\frac{dv_i^{(I)}}{dt} = k\left(v_i^{(I)} - v_r\right)\left(v_i^{(I)} - v_t\right) - u_i^{(I)} + I_{DC} + D\xi_i^{(I)} - I_{I,i}^{(\text{intra,syn})} - I_{I,i}^{(\text{inter,syn})}, \tag{1}$$

$$\frac{du_i^{(I)}}{dt} = a\left\{U\left(v_i^{(I)}\right) - u_i^{(I)}\right\}, \quad i = 1,\ldots,L, \quad I = 1,\ldots,M, \tag{2}$$

with the auxiliary afterspike resetting,

$$\text{if } v_i^{(I)} \geqslant v_p, \quad \text{then } v_i^{(I)} \leftarrow c \quad \text{and } u_i^{(I)} \leftarrow u_i^{(I)} + d, \tag{3}$$

where

$$U(v) = \begin{cases} 0 & \text{for } v < v_b, \\ b(v - v_b)^3 & \text{for } v \geqslant v_b, \end{cases} \tag{4}$$

$$I_{I,i}^{(\text{intra,syn})} = \frac{J_{\text{intra}}}{d_{I,i}^{\text{intra}}} \sum_{j=1(\neq i)}^{L} w_{ij}^{(I,I)} s_j^{(I)}(t)\left(v_i^{(I)} - V_{\text{syn}}\right), \tag{5}$$

$$I_{I,i}^{(\text{inter,syn})} = \frac{J_{\text{inter}}}{d_{I,i}^{\text{inter}}} \sum_{J=1(\neq I)}^{M} \sum_{j=1}^{L} w_{ij}^{(I,J)} s_j^{(J)}(t)\left(v_i^{(I)} - V_{\text{syn}}\right), \tag{6}$$

$$s_j^{(I)}(t) = \sum_{f=1}^{F_j^{(I)}} E\left(t - t_f^{(I,j)} - \tau_l\right); \quad E(t) = \frac{1}{\tau_d - \tau_r}\left(e^{-t/\tau_d} - e^{-t/\tau_r}\right)\Theta(t). \tag{7}$$

TABLE I. Parameter values used in our computations for Figs. 2–10; units of the capacitance, the potential, the current, and the time are pF, mV, pA, and ms, respectively.

(1)	Single Izhikevich FS interneurons [74]				
	$C = 20$	$v_r = -55$	$v_t = -40$	$v_p = 25$	$v_b = -55$
	$k = 1$	$a = 0.2$	$b = 0.025$	$c = -45$	$d = 0$
(2)	External stimulus to Izhikevich FS interneurons				
	$I_{dc} = 1500$	$D = 500$			
(3)	Inhibitory GABAergic synapse [15]				
	$\tau_l = 1$	$\tau_r = 0.5$	$\tau_d = 5$	$V_{\rm syn} = -80$	
(4)	Intramodular coupling in small-world subnetworks				
	$M_{\rm syn}^{\rm (intra)} = 50$	$J_{\rm intra} = 1400$	$p_{\rm rewiring}$: varying		
(5)	Intermodular connection				
	$M_{\rm syn}^{\rm (inter)}$: varying	$J_{\rm inter}$: varying			

Here $v_i^{(I)}(t)$ and $u_i^{(I)}(t)$ are the state variables of the ith interneuron in the Ith subnetwork at a time t, which represent the membrane potential and the recovery current, respectively. The membrane potential and the recovery variable, $v_i^{(I)}(t)$ and $u_i^{(I)}(t)$, are reset according to Eq. (3) when $v_i^{(I)}(t)$ reaches its cutoff value v_p. C, v_r, and v_t in Eq. (1) are the membrane capacitance, the resting membrane potential, and the instantaneous threshold potential, respectively. The parameter values used in our computations are listed in Table I. More details on the FS Izhikevich interneuron model, the external stimulus to the FS interneuron, the intramodular and the intermodular synaptic currents, and numerical integration of the governing equations are given in the following sections.

1. FS Izhikevich interneuron model

The Izhikevich model matches neuronal dynamics by tuning the parameters (k,a,b,c,d) instead of matching neuronal electrophysiology, in contrast to Hodgkin-Huxley-type conductance-based models. The parameters k and b are related to the neuron's rheobase and input resistance, and a, c, and d are the recovery time constant, the afterspike reset value of v, and the total amount of outward minus inward currents during the spike and affecting the afterspike behavior (i.e., afterspike jump value of u), respectively. Depending on the values of these parameters, the Izhikevich neuron model may exhibit 20 of the most prominent neurocomputational features of cortical neurons [72–75]. Here we use the parameter values for the FS interneurons in the layer 5 rat visual cortex, which are listed in the first item of Table I.

2. External stimulus to the FS Izhikevich interneuron

Each Izhikevich interneuron is stimulated by both a common dc current I_{dc} and an independent Gaussian white noise $\xi_i^{(I)}$, as shown in the third and the fourth terms in Eq. (1). The Gaussian white noise satisfies $\langle \xi_i^{(I)}(t) \rangle = 0$ and $\langle \xi_i^{(I)}(t) \xi_j^{(J)}(t') \rangle = \delta_{IJ}\delta_{ij}\delta(t-t')$, where $\langle \cdots \rangle$ denotes the ensemble average. Here the Gaussian noise ξ is a parametric one that randomly perturbs the strength of the applied current I_{dc}, and its intensity is controlled by the parameter D. For $D = 0$, the Izhikevich interneuron exhibits a jump from a resting state to a spiking state via subcritical Hopf bifurcation for a higher threshold $I_{dc,h}(\simeq 73.7)$ by absorbing an unstable limit cycle born via a fold limit cycle bifurcation at a lower threshold $I_{dc,l}(\simeq 72.8)$. Therefore, the Izhikevich interneuron shows type-II excitability since it begins to fire with a nonzero frequency [76,77]. With increasing I_{dc} from $I_{dc,h}$, the mean firing rate f increases monotonically. The values of I_{dc} and D used in this paper are given in the second item of Table I.

3. Intramodular and intermodular synaptic currents

The last two terms in Eq. (1) represent the intra- and the intermodular synaptic couplings of inhibitory FS interneurons. $I_{I,i}^{\rm (intra,syn)}$ and $I_{I,i}^{\rm (inter,syn)}$ of Eqs. (5) and (6) represent the intra- and the intermodular synaptic currents injected into the ith neuron in the Ith subnetwork, respectively. The synaptic connectivity is given by the connection weight matrix W $(=\{w_{ij}^{(I,J)}\})$, where $w_{ij}^{(I,J)} = 1$ if the neuron j in the Jth subnetwork is presynaptic to the neuron i in the Ith subnetwork; otherwise, $w_{ij}^{(I,J)} = 0$. Here the intramodular synaptic connection is modeled in terms of the Watts-Strogatz small-world network. Then the in-degree of the ith neuron in the Ith subnetwork for the intramodular synaptic connection, $d_{I,i}^{\rm intra}$ (i.e., the number of intramodular synaptic inputs to the neuron i in the Ith subnetwork) is given by $d_{I,i}^{\rm intra} = \sum_{j=1(\neq i)}^{L} w_{ij}^{(I,I)}$. For this intramodular case, the average number of intramodular synaptic inputs per neuron is $M_{\rm syn}^{\rm (intra)} = \frac{1}{ML}\sum_{I=1}^{M}\sum_{i=1}^{L} d_{I,i}^{\rm intra}$. In contrast to the intramodular connection, the intermodular synaptic connection is given randomly. Then the in-degree of the ith neuron in the Ith subnetwork for the intermodular synaptic connection, $d_{I,i}^{\rm inter}$ (i.e., the number of intermodular synaptic inputs to the neuron i in the Ith subnetwork) is given by $d_{I,i}^{\rm inter} = \sum_{J=1(\neq I)}^{M}\sum_{j=1}^{L} w_{ij}^{(I,J)}$. In the intermodular case, the average number of intermodular synaptic inputs per neuron is $M_{\rm syn}^{\rm (inter)} = \frac{1}{ML}\sum_{I=1}^{M}\sum_{i=1}^{L} d_{I,i}^{\rm inter}$, and these intermodular links are randomly connected with the intermodular connection probability $p_{\rm inter} = \frac{M_{\rm syn}^{\rm (inter)}}{(M-1)L}$. Compared to the intramodular connections, the intermodular connections are sparse (i.e., $M_{\rm syn}^{\rm (inter)} < M_{\rm syn}^{\rm (intra)}$). The fraction of open synaptic ion channels at time t is denoted by $s(t)$. The time course of $s_j^{(I)}(t)$ of the jth neuron in the Ith subnetwork is given by a sum of delayed double-exponential functions $E(t - t_f^{(I,j)} - \tau_l)$ [see Eq. (7)], where τ_l is the synaptic delay, and $t_f^{(I,j)}$ and $F_j^{(I)}$ are the fth spiking time and the total number of spikes of the jth neuron in the Ith subnetwork at time t, respectively. Here $E(t)$ [which corresponds to contribution of a presynaptic spike occurring at

time 0 to $s(t)$ in the absence of synaptic delay] is controlled by the two synaptic time constants, synaptic rise time τ_r and decay time τ_d, and $\Theta(t)$ is the Heaviside step function, $\Theta(t) = 1$ for $t \geqslant 0$ and 0 for $t < 0$. The intra- and the intermodular synaptic coupling strengths are controlled by the parameters J_{intra} and J_{inter}, respectively, and V_{syn} is the synaptic reversal potential. For the inhibitory GABAergic synapse (involving the GABA_A receptors), the values of τ_l, τ_r, τ_d, and V_{syn} are listed in the third item of Table I.

4. Numerical method

Numerical integration of stochastic differential Eqs. (1) and (2) is done by employing the Heun method [78] with the time step $\Delta t = 0.01$ ms. For each realization of the stochastic process, we choose a random initial point $[v_i^{(I)}(0), u_i^{(I)}(0)]$ for the ith ($i = 1, \ldots, N$) neuron in the Ith subnetwork with uniform probability in the range of $v_i^{(I)}(0) \in (-50, -45)$ and $u_i^{(I)}(0) \in (10, 15)$.

III. METHODS FOR CHARACTERIZATION OF INDIVIDUAL AND POPULATION STATES IN CLUSTERED NETWORKS

In the following sections, we explain methods used to characterize individual and population states in clustered networks. Particularly, the emergence of population synchronization and its degree are characterized by employing realistic measures, based on instantaneous sub- and whole-population spike rates [71]. Furthermore, we introduce a realistic cross-correlation modularity measure, denoting the matching degree between the instantaneous subpopulation spike rates to examine whether the population synchronization is global or modular.

A. Characterization of individual firing behaviors

Firing behaviors of individual interneurons are characterized in terms of the interspike interval (ISI) histogram and the mean firing rate (MFR) distribution. The ISI histogram is composed of 5×10^4 ISIs (obtained from all the interneurons), and the bin size for the histogram is 0.5 ms. The MFR for each interneuron is calculated by following the membrane potential during the averaging time of 2×10^4 ms after discarding the transient time of 10^3 ms, and the bin size for the histogram is 2 Hz.

B. Sub- and whole-population variables

In computational neuroscience, an ensemble-averaged subpopulation potential $V_s^{(I)}(t)$ for the Ith subnetwork ($I = 1,2,3$), containing L FS Izhikevich interneurons,

$$V_s^{(I)}(t) = \frac{1}{L} \sum_{i=1}^{L} v_i^{(I)}(t), \tag{8}$$

and an ensemble-averaged whole-population potential for the whole network with M (=3) subnetworks,

$$V_w(t) = \frac{1}{M} \sum_{I=1}^{M} V_s^{(I)}(t), \tag{9}$$

are often used for describing the emergence of population neural synchronization in the sub- and the whole populations, respectively (e.g., sparse synchronization in a population of subthreshold neurons was described in terms of an ensemble-averaged global potential [19–21]). However, to directly obtain $V_s^{(I)}(t)$ and $V_w(t)$ in real experiments is very difficult. To overcome this difficulty, instead of $V_s^{(I)}(t)$ and $V_w(t)$, we use experimentally obtainable instantaneous sub- and whole-population spike rates which are often used as collective quantities showing sub- and whole-population behaviors [3,13–18,64,70,71]. The instantaneous subpopulation spike rate (ISPSR) $R_s^{(I)}(t)$ is obtained from the raster plot of neural spikes, which is a collection of spike trains of individual neurons in the Ith subpopulation. Such raster plots of spikes, where subpopulation spike synchronization may be well visualized, are fundamental data in experimental neuroscience. For the synchronous case, "stripes" (composed of spikes and indicating subpopulation synchronization) are found to be formed in the raster plot. Hence, for a synchronous case, an oscillating ISPSR appears, while for an unsynchronized case the ISPSR is nearly stationary. To obtain a smooth ISPSR, we employ the kernel density estimation (kernel smoother) [79]. Each spike in the raster plot is convoluted (or blurred) with a kernel function $K_h(t)$ to obtain a smooth estimate of ISPSR for the Ith subnetwork, $R_s^{(I)}(t)$,

$$R_s^{(I)}(t) = \frac{1}{L} \sum_{i=1}^{L} \sum_{s=1}^{n_i^{(I)}} K_h\left(t - t_s^{(I,i)}\right), \tag{10}$$

where $t_s^{(I,i)}$ is the sth spiking time of the ith neuron in the Ith subnetwork, $n_i^{(I)}$ is the total number of spikes for the ith neuron in the Ith subnetwork, and we use a Gaussian kernel function of band width h:

$$K_h(t) = \frac{1}{\sqrt{2\pi}h} e^{-t^2/2h^2}, \quad -\infty < t < \infty. \tag{11}$$

Throughout the paper, the bandwidth of the Gaussian kernel estimate is $h = 1$ ms. Then the instantaneous whole-population spike rate (IWPSR) kernel estimate $R_w(t)$ for the whole population is given by an average of the ISPSR kernel estimates of the M(=3) subpopulations:

$$R_w(t) = \frac{1}{M} \sum_{I=1}^{M} R_s^{(I)}(t). \tag{12}$$

Moreover, for the synchronous case, the subpopulation frequency $f_p^{(I)}$ of the regularly oscillating ISPSR $R_s^{(I)}(t)$ may be obtained from the one-sided power spectrum of $\Delta R_s^{(I)}(t)$ $[= R_s^{(I)}(t) - \overline{R_s^{(I)}(t)}]$ with the mean-squared amplitude normalization. The number of data for the power spectrum is 2^{13}, and the overline denotes the time average.

C. Sub- and whole-population order parameters

As is well known, a conventional order parameter, based on the ensemble-averaged global potential, is often used for describing transition from synchronization to unsynchronization in computational neuroscience [19–21,80–82]. Recently, instead of the global potential, we used an experimentally obtainable instantaneous population spike rate kernel estimate

and developed a realistic order parameter for the case of the nonmodular networks, which may be applicable in both the computational and the experimental neuroscience [71]. For the case of modular networks, the mean-square deviation of the ISPSR kernel estimate $R_s^{(I)}(t)$ for the Ith subnetwork ($I = 1, 2, 3$),

$$\mathcal{O}_s^{(I)} \equiv \overline{\left[R_s^{(I)}(t) - \overline{R_s^{(I)}(t)}\right]^2}, \tag{13}$$

and the mean-square deviation of the IWPSR kernel estimate $R_w(t)$ for the whole network,

$$\mathcal{O}_w \equiv \overline{[R_w(t) - \overline{R_w(t)}]^2}, \tag{14}$$

play the role of realistic sub- and whole-population order parameters $\mathcal{O}_s^{(I)}$ and $\mathcal{O}_w$ to determine a threshold for the synchronization-unsynchronization transition, where the overbar represents the time average. Here each order parameter is obtained through average over 20 realizations, and the averaging time for the calculation of the order parameter in each realization is 4×10^3 ms. Then the order parameters $\mathcal{O}_s^{(I)}$ and $\mathcal{O}_w$, representing the time-averaged fluctuations of $R_s^{(I)}(t)$ and $R_w(t)$, approach nonzero (zero) limit values for the synchronized (unsynchronized) state in the thermodynamic limit of $L \to \infty$. These order parameters may be regarded as thermodynamic measures because they concern just the macroscopic ISPSR and IWPSR kernel estimates $R_s^{(I)}(t)$ and $R_w(t)$ without any consideration between the macroscopic ISPSR and IWPSR kernel estimates and microscopic individual spikes.

D. Spatial cross-correlation functions

To further understand the synchronization-unsynchronization transition, we consider the "microscopic" dynamical cross correlations between neuronal pairs. For obtaining dynamical pair cross correlations, each spike train of the ith neuron in the Ith subnetwork is convoluted with a Gaussian kernel function $K_h(t)$ of band width h to get a smooth estimate of instantaneous individual spike rate (IISR) $r_i^{(I)}(t)$,

$$r_i^{(I)}(t) = \sum_{s=1}^{n_i^{(I)}} K_h\left(t - t_s^{(I,i)}\right), \tag{15}$$

where $t_s^{(I,i)}$ is the sth spiking time of the ith neuron in the Ith subnetwork, $n_i^{(I)}$ is the total number of spikes for the ith neuron, and $K_h(t)$ is given in Eq. (11). Then the normalized temporal cross-correlation function $C_{i,j}^{(I)}(\tau)$ between the IISR kernel estimates $r_i^{(I)}(t)$ and $r_j^{(I)}(t)$ of the (i, j) neuronal pair in the Ith subnetwork is given by

$$C_{i,j}^{(I)}(\tau) = \frac{\overline{\Delta r_i^{(I)}(t+\tau)\Delta r_j^{(I)}(t)}}{\sqrt{\overline{\Delta r_i^{(I)2}(t)}}\sqrt{\overline{\Delta r_j^{(I)2}(t)}}}, \tag{16}$$

where $\Delta r_i^{(I)}(t) = r_i^{(I)}(t) - \overline{r_i^{(I)}(t)}$ and the overline denotes the time average. Here the number of data used for the calculation of each temporal cross-correlation function $C_{i,j}^{(I)}(\tau)$ is 4×10^3. Similar to the case of nonmodular small-world network [64], we introduce the spatial cross-correlation function $C_l^{(I)}$ ($l = 1, \ldots, L/2$) between neuronal pairs separated by a spatial distance l in the Ith subnetwork through average of all the temporal cross correlations between $r_i^{(I)}(t)$ and $r_{i+l}^{(I)}(t)$ ($i = 1, \ldots, L$) at the zero-time lag:

$$C_l^{(I)} = \frac{1}{L}\sum_{i=1}^{L} C_{i,i+l}^{(I)}(0) \quad \text{for} \quad l = 1, \ldots, L/2. \tag{17}$$

Here if $i + l > L$ in Eq. (17), then $i + l - L$ is considered instead of $i + l$ because neurons lie on the ring. If the spatial cross-correlation function $C_l^{(I)}$ ($l = 1, \ldots, L/2$) is nonzero in the whole range of l, then the spatial correlation length η_I becomes $L/2$ (note that the maximal distance between neurons is $L/2$ because of the ring architecture on which neurons exist) covering the whole subnetwork. For this case, synchronization appears in the subnetwork; otherwise, unsynchronization occurs.

E. Cross-correlation modularity measure

To determine the type of synchronization (modular or global) in modular networks, we measure the matching degree between the intramodular dynamics of subnetworks in terms of the cross-correlation modularity measure C_M, based on ISPSRs. The normalized temporal cross-correlation function $C_{I,J}(\tau)$ between the ISPSR kernel estimates $R_s^{(I)}(t)$ and $R_s^{(J)}(t)$ of the Ith and the Jth subnetworks is given by

$$C_{I,J}(\tau) = \frac{\overline{\Delta R_s^{(I)}(t+\tau)\Delta R_s^{(J)}(t)}}{\sqrt{\overline{\Delta R_s^{(I)2}(t)}}\sqrt{\overline{\Delta R_s^{(J)2}(t)}}}, \tag{18}$$

where $\Delta R_s^{(I)}(t) = R_s^{(I)}(t) - \overline{R_s^{(I)}(t)}$ and the overline denotes the time average. Figures 6(c1)–6(c5) show the normalized temporal cross-correlation functions $C_{I,J}(\tau)$ for $J_{\text{inter}} = 10$, 30, 70, 400, and 1200, respectively. Then, the cross-correlation modularity measure C_M is obtained through average of the temporal cross correlations between all the subpopulation pairs at the zero-time lag:

$$C_M = \frac{2}{M(M-1)}\sum_{I=1}^{M-1}\sum_{J=I+1}^{M} C_{I,J}(0). \tag{19}$$

Here the cross-correlation modularity measure $\langle C_M \rangle_r$ is obtained through average over 20 realizations, and the number of data used for the calculation of each temporal cross-correlation function $C_{I,J}(\tau)$ in each realization is 4×10^3.

F. State diagram

Population states vary depending on the intermodular connection parameters J_{inter} and $M_{\text{syn}}^{(\text{inter})}$, which may be well shown in the state diagram in the J_{inter}-$M_{\text{syn}}^{(\text{inter})}$ plane. To obtain the state diagram, we first divide the J_{inter}-$M_{\text{syn}}^{(\text{inter})}$ plane into the 20×10 grids. Then, at each grid point, we calculate the subpopulation order parameters $\mathcal{O}_s^{(I)}$ ($I = 1,2,3$) for $L = 10^3$ and 10^4 to determine whether the population state at the grid point is synchronized or unsynchronized. If $\mathcal{O}_s^{(I)}$ for $L = 10^4$ is smaller than $f\mathcal{O}_s^{(I)}$ for $L = 10^3$ (f is some appropriate factor less than unity; for convenience we set $f = 0.3$), $\mathcal{O}_s^{(I)}$

is expected to decrease with increasing L. For the case of decrease in $\mathcal{O}_s^{(I)}$ with increasing L, unsynchronization occurs at the grid point; otherwise, synchronization appears. Next, at the grid points where synchronization occurs, we calculate the cross-correlation modularity measure C_M to determine whether the population synchronization is modular or global. If C_M is larger than a threshold C_M^{th} (in our computation, we set $C_M^{th} = 0.995$), global synchronization is expected to appear at the grid point; otherwise, modular synchronization occurs. After determining the population states (modular or global synchronization and unsynchronization) at all grid points, we try to obtain the synchronization-unsynchronization and the modular-global synchronization transition curves accurately. To this end, we calculate $\mathcal{O}_s^{(I)}$ (C_M) in the small parameter region between the synchronization and unsynchronization (the modular and global synchronization) grid points by varying $J_{\rm inter}$ or $M_{\rm syn}^{\rm (inter)}$. Moreover, to get more accurate transition curves, we divide a part of the parameter plane where the transition curves change rapidly into more minute grids and repeat the above computations.

G. Sub- and whole-population statistical-mechanical spiking measures

We measure the degree of modular and global sparse synchronization in terms of realistic statistical-mechanical sub- and whole-population spiking measures, based on the ISPSR and the IWPSR kernel estimates $R_s^{(I)}(t)$ and $R_w(t)$ [71]. Spike synchronization may be well visualized in the raster plots of spikes. For a synchronized case, the raster plot is composed of partially occupied stripes (indicating sparse synchronization), and the corresponding ISPSR and IWPSR kernel estimates, $R_s^{(I)}(t)$ ($I = 1,2,3$) and $R_w(t)$, exhibit regular oscillations. Each ith ($i = 1,2,3,\ldots$) global cycles of $R_s^{(I)}(t)$ and $R_w(t)$ begin from their left minimum, pass the central maximum, and end at the right minimum [also, corresponding to the beginning point of the next $(i+1)$th global cycles]; the first global cycles of $R_s^{(I)}(t)$ and $R_w(t)$ appear after transient times of 10^3 ms, respectively. Spikes which appear in the ith global cycles of $R_s^{(I)}(t)$ and $R_w(t)$ form the ith stripes in the raster plots for the sub- and the whole populations, respectively. To measure the degree of the sub- and the whole-population spike synchronization seen in the raster plots, statistical-mechanical sub- and whole-population measures $M_s^{(I)}$ and $M_s^{(w)}$, based on $R_s^{(I)}(t)$ and $R_w(t)$, are introduced by considering the occupation pattern and the pacing pattern of spikes in the stripes for the sub- and the whole populations, which corresponds to a simple extension of the case of nonmodular networks [71]. The sub- and the whole-population spiking measures $M_i^{(I)}$ ($I = 1,\ 2,\ 3$) and $M_i^{(w)}$ of the ith stripes [appearing in the ith global cycles of $R_s^{(I)}(t)$ and $R_w(t)$] are defined by the products of the sub- and the whole-population occupation degrees $O_i^{(I)}$ and $O_i^{(w)}$ of spikes (representing the density of the ith stripes) and the sub- and the whole-population pacing degrees $P_i^{(I)}$ and $P_i^{(w)}$ of spikes (denoting the smearing of the ith stripes), respectively:

$$M_i^{(I)} = O_i^{(I)} P_i^{(I)} \ \text{ and } \ M_i^{(w)} = O_i^{(w)} P_i^{(w)}. \tag{20}$$

The sub- and the whole-population occupation degrees $O_i^{(I)}$ and $O_i^{(w)}$ in the ith stripes are given by the fractions of spiking neurons in the ith stripes,

$$O_i^{(I)} = \frac{N_{I,i}^{(s)}}{L} \ \text{ and } \ O_i^{(w)} = \frac{N_{w,i}^{(s)}}{ML}, \tag{21}$$

where $N_{I,i}^{(s)}$ and $N_{w,i}^{(s)}$ are the numbers of spiking neurons in the ith stripes for the Ith subnetwork and the whole network, respectively. For sparse synchronization with partially occupied stripes, $O_i^{(I)} \ll 1$ and $O_i^{(w)} \ll 1$. The pacing degrees $P_i^{(I)}$ and $P_i^{(w)}$ of sparse spikes in the ith stripes for the sub- and the whole-populations can be determined in a statistical-mechanical way by taking into account their contributions to the macroscopic ISPSR and IWPSR kernel estimates $R_s^{(I)}(t)$ and $R_w(t)$, respectively. Instantaneous global phases $\Phi_s^{(I)}(t)$ of $R_s^{(I)}(t)$ and $\Phi_w(t)$ of $R_w(t)$ are introduced via linear interpolation in the two successive subregions forming global cycles [71]. The global phases $\Phi_s^{(I)}(t)$ and $\Phi_w(t)$ between the left minimum (corresponding to the beginning point of the ith global cycle) and the central maximum are given by

$$\Phi_s^{(I)}(t) = 2\pi(i-3/2) + \pi\left(\frac{t - t_{I,i}^{(\min)}}{t_{I,i}^{(\max)} - t_{I,i}^{(\min)}}\right) \quad \text{for } t_{I,i}^{(\min)} \leqslant t < t_{I,i}^{(\max)}, \tag{22}$$

$$\Phi_w(t) = 2\pi(i-3/2) + \pi\left(\frac{t - t_{w,i}^{(\min)}}{t_{w,i}^{(\max)} - t_{w,i}^{(\min)}}\right) \quad \text{for } t_{w,i}^{(\min)} \leqslant t < t_{w,i}^{(\max)}, \tag{23}$$

and $\Phi_s^{(I)}(t)$ and $\Phi_w(t)$ between the central maximum and the right minimum [corresponding to the beginning point of the $(i+1)$th global cycle] are given by

$$\Phi_s^{(I)}(t) = 2\pi(i-1) + \pi\left(\frac{t - t_{I,i}^{(\max)}}{t_{I,i+1}^{(\min)} - t_{I,i}^{(\max)}}\right) \quad \text{for } t_{I,i}^{(\max)} \leqslant t < t_{I,i+1}^{(\min)}, \tag{24}$$

$$\Phi_w(t) = 2\pi(i-1) + \pi\left(\frac{t - t_{w,i}^{(\max)}}{t_{w,i+1}^{(\min)} - t_{w,i}^{(\max)}}\right) \quad \text{for } t_{w,i}^{(\max)} \leqslant t < t_{w,i+1}^{(\min)}, \tag{25}$$

where $t_{I,i}^{(\min)}$ and $t_{w,i}^{(\min)}$ are the beginning times of the ith ($i = 1,2,3,\ldots$) global cycles of $R_s^{(I)}(t)$ and $R_w(t)$ [i.e., the times at which the left minima of $R_s^{(I)}(t)$ and $R_w(t)$ appear in the ith global cycles], respectively, and $t_{I,i}^{(\max)}$ and $t_{w,i}^{(\max)}$ are the times at which the maxima of $R_s^{(I)}(t)$ and $R_w(t)$ appear in the ith global cycles, respectively. Then, the contributions of the kth microscopic spikes in the ith stripes occurring at the times $t_{I,k}^{(s)}$ and $t_{w,k}^{(s)}$ to $R_s^{(I)}(t)$ and $R_w(t)$ are given by $\cos\Phi_k^{(I)}$ and $\cos\Phi_k^{(w)}$, where $\Phi_k^{(I)}$ and $\Phi_k^{(w)}$ are the global phases at the kth spiking times [i.e., $\Phi_k^{(I)} \equiv \Phi_s^{(I)}(t_{I,k}^{(s)})$ and $\Phi_k^{(w)} \equiv \Phi_w(t_{w,k}^{(s)})$]. Microscopic spikes make the most constructive (in-phase) contributions to $R_s^{(I)}(t)$ and $R_w(t)$ when the corresponding global phases $\Phi_k^{(I)}$ and $\Phi_k^{(w)}$ are $2\pi n$ ($n = 0,1,2,\ldots$), while they make the most destructive (antiphase) contribution to $R_s^{(I)}(t)$ and $R_w(t)$ when $\Phi_k^{(I)}$ and $\Phi_k^{(w)}$ are $2\pi(n-1/2)$. By averaging the contributions of all microscopic spikes in the ith stripes to $R_s^{(I)}(t)$ and $R_w(t)$, we obtain the pacing degrees $P_i^{(I)}$ and $P_i^{(w)}$ of spikes in the ith stripes,

$$P_i^{(I)} = \frac{1}{S_i^{(I)}} \sum_{k=1}^{S_i^{(I)}} \cos\Phi_k^{(I)} \quad \text{and} \quad P_i^{(w)} = \frac{1}{S_i^{(w)}} \sum_{k=1}^{S_i^{(w)}} \cos\Phi_k^{(w)}, \tag{26}$$

where $S_i^{(I)}$ and $S_i^{(w)}$ are the total numbers of microscopic spikes in the ith stripes for the sub- and the whole population, respectively. By averaging $M_i^{(I)}$ and $M_i^{(w)}$ of Eq. (20) over a sufficiently large number N_s of stripes, we obtain the sub- and whole-population statistical-mechanical spiking measures $M_s^{(I)}$ and $M_s^{(w)}$:

$$M_s^{(I)} = \frac{1}{N_s} \sum_{i=1}^{N_s} M_i^{(I)} \quad \text{and} \quad M_s^{(w)} = \frac{1}{N_s} \sum_{i=1}^{N_s} M_i^{(w)}. \tag{27}$$

Here we follow 3×10^3 global cycles in each realization, and obtain average occupation degrees, average pacing degrees, and average statistical-mechanical spiking measures via average over 20 realizations.

IV. EFFECT OF INTERMODULAR CONNECTION ON FAST SPARSELY SYNCHRONIZED RHYTHMS

In this section, we investigate the effect of intermodular connection on the emergence of fast sparsely synchronized rhythms by varying both the intermodular coupling strength J_{inter} and the average number of intermodular links per interneuron $M_{\text{syn}}^{(\text{inter})}$ in the clustered small-world network of inhibitory FS Izhikevich interneurons. In contrast to the case of nonmodular networks, two kinds of sparsely synchronized states such as modular and global sparse synchronization are thus found. These sparsely synchronized states are characterized by employing diverse realistic measures, explained in Sec. III.

In the absence of intermodular coupling, we consider three cases of the intramodular dynamics in the Watts-Strogatz small-world subnetworks: (1) synchronized in all identical subnetworks, (2) unsynchronized in all identical subnetworks, and (3) synchronized and/or unsynchronized in nonidentical subnetworks. For each case, we study the emergence of sparsely synchronized population states by changing both J_{inter} and $M_{\text{syn}}^{(\text{inter})}$ for a fixed set of I_{dc}, D, $M_{\text{syn}}^{(\text{intra})}$, and $J_{\text{syn}}^{(\text{intra})}$ (whose values are listed in Table I). In Sec. IV A, we start from the first case of intramodular dynamics. To further examine dependence on the type of intramodular dynamics, we also study the second and the third cases in the Sec. IV B.

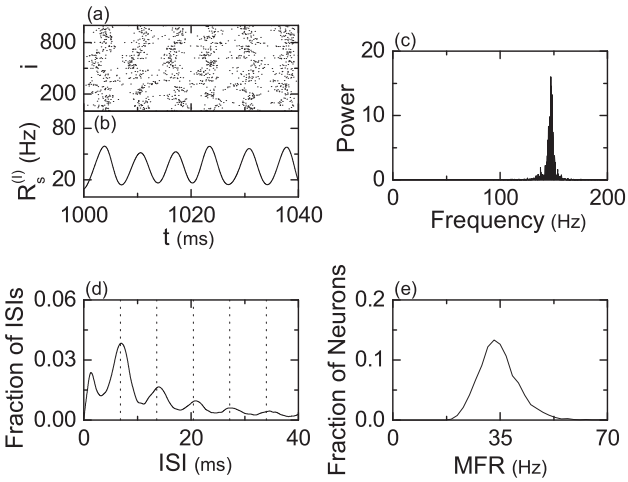

FIG. 2. Fast sparse synchronization in identical small-world subnetworks with $p_{\text{rewiring}} = 0.25$ (case 1) in the absence of intermodular coupling. (a) Raster plot of neural spikes and (b) ISPSR kernel estimate $R_s^{(I)}(t)$. (c) One-sided power spectrum of $\Delta R_s^{(I)}(t)$ [$=R_s^{(I)}(t) - \overline{R_s^{(I)}(t)}$] with the mean-squared amplitude normalization. (d) Interspike interval (ISI) histogram for the individual interneurons; the vertical dotted lines denote integer multiples of the global period T_I ($\simeq$6.8 ms) of $R_s^{(I)}(t)$. (e) MFR (mean firing rate) distribution of individual interneurons.

A. First case of intramodular dynamics: Synchronized in all identical subnetworks

In this section, we consider the first case of intramodular dynamics which are synchronized in three identical small-world subnetworks with the same rewiring probability $p_{\text{rewiring}} = 0.25$. In the absence of intermodular coupling (i.e., $J_{\text{inter}} = 0$), every subpopulation in the small-world subnetworks exhibits identical sparse synchronization, as shown in Fig. 2. Clear stripes are formed in the raster plot of Fig. 2(a). The density of stripes is sparse because only a small fraction (about 0.22) of the total L ($=10^3$) neurons in the subpopulation fire in each stripe. Due to presence of these sparse stripes, the ISPSR kernel estimate $R_s^{(I)}(t)$ shows fast regular oscillation with subpopulation frequency $f_p^{(I)} \simeq 147$ Hz, as shown in Figs. 2(b)–2(c). For the case of individual neurons, the ISI histogram has multiple peaks appearing at multiples of the period T_I ($\simeq$6.8 ms) of $R_s^{(I)}(t)$ (i.e., skipping of spikes occurs at random integer multiples of T_I) [see Fig. 2(d)]. Because of this stochastic spike skipping (also called the stochastic phase locking) [19–21,64,70,71,83–85], individual neurons exhibit stochastic and intermittent spike discharges; hence, partial occupation occurs in the stripes of the raster plot. In contrast to subpopulation rhythms, the distribution of MFRs of individual neurons shows a peak near $f_i^{(I)}$ ($\simeq$33 Hz) which is much less than the subpopulation frequency $f_p^{(I)}$ [see

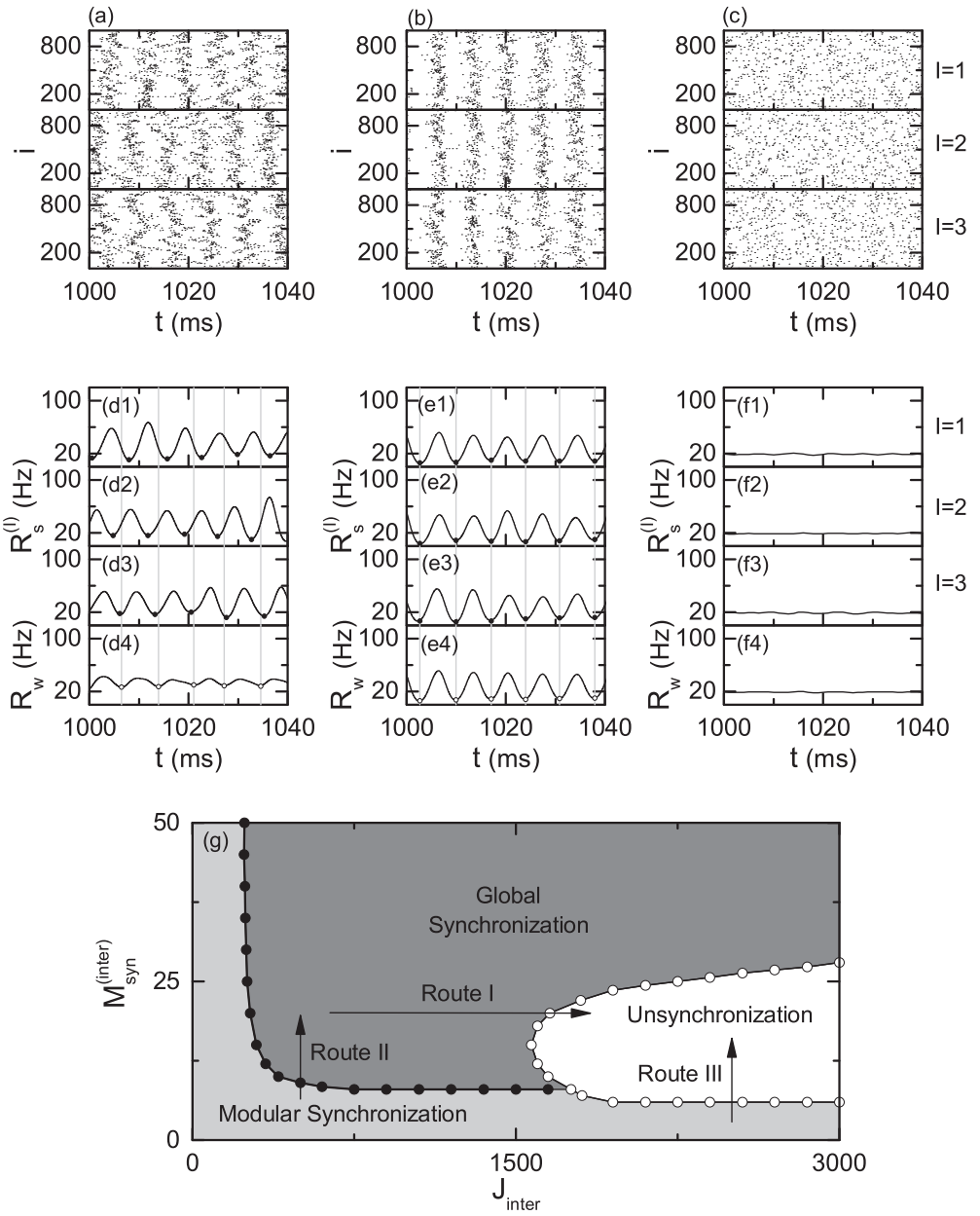

FIG. 3. Modular and global sparse synchronization for the first case of intramodular dynamics with $p_{\text{rewiring}} = 0.25$. $M_{\text{syn}}^{(\text{inter})} = 20$ in (a)–(f4). Raster plots of neural spikes in the subnetworks ($I = 1,2,3$) for $J_{\text{inter}} = 10$ (a), 500 (b), and 2500 (c). Instantaneous sub- and whole-population spike rate kernel estimates, $R_s^{(I)}(t)$ ($I = 1,2,3$) and $R_w(t)$: $J_{\text{inter}} = 10$ (d1)–(d4), 500 (e1)–(e4), and 2500 (f1)–(f4). Vertical gray lines for $J_{\text{inter}} = 10$ and 500 pass minima of $R_w(t)$, and the minima of $R_s^{(I)}(t)$ [$R_w(t)$] are denoted by solid (open) circles. (g) State diagram in the J_{inter}-$M_{\text{syn}}^{(\text{inter})}$ plane.

Fig. 2(e)]. In this way, firing activity of individual neurons differs distinctly from the population oscillatory behavior for the case of sparse synchronization [3,13–18,64,70,71]. For more details on the sparse synchronization in the (nonmodular) small-world network, refer to [64].

From now on, we employ the methods for characterizing population dynamics in Sec. III and investigate the effect of intermodular connection on sparse synchronization by changing the intermodular coupling strength J_{inter} for $M_{\text{syn}}^{(\text{inter})} = 20$. Figures 3(a)–3(c) show the raster plots of spikes in the three subpopulations for $J_{\text{inter}} = 10$, 500, and 2500, respectively. The corresponding ISPSR and IWPSR kernel estimates, $R_s^{(I)}(t)$ and $R_w(t)$ of Eqs. (10) and (12), for $J_{\text{inter}} = 10$, 500, and 2500 are also shown in Figs. 3(d1)–3(f4), respectively. For small J_{inter}, the intermodular coupling strength plays a constructive role to favor the pacing between spikes in each subnetwork, as shown in the case of $J_{\text{inter}} = 10$. For each Ith subpopulation, sparse stripes are formed in the raster plot and $R_s^{(I)}(t)$ shows a regular oscillation, as shown in Figs. 3(a) and 3(d1)–3(d4). Hence, each subpopulation exhibits sparse synchronization. However, the intramodular dynamics of subnetworks make some mismatching because both the stripes and the ISPSRs between the subnetworks are shifted. Vertical gray lines which pass minima of $R_w(t)$ are drawn as reference

lines for matching between $R_s^{(I)}(t)$ $(I = 1,2,3)$ [where the minima of $R_s^{(I)}(t)$ [$R_w(t)$] are denoted by solid (open) circles]. As a result of mismatching, the degree of sparse synchronization in the whole population becomes less than that in the subnetworks [i.e., the amplitude of $R_w(t)$ is less than that of $R_s^{(I)}(t)$], and this kind of population behavior for $J_{\rm inter} = 10$ is referred to as the modular sparse synchronization because it reveals the modular structure. With increasing $J_{\rm inter}$, the mismatching degree between the intramodular dynamics of subnetworks decreases, although the stripes in the raster plots become more sparse due to increased inhibition. Eventually, when passing a threshold $J_{\rm inter}^*$ ($\simeq$268), intramodular dynamics of subnetworks begin to make perfect matching. As a result, the population behavior becomes globally identical, independently of the cluster structure, as shown in Figs. 3(b) and 3(e1)–3(e4) for $J_{\rm inter} = 500$ [where all the minima of $R_s^{(I)}(t)(I = 1,2,3)$ lie on the reference vertical line passing the minima of $R_w(t)$], and it is referred to as the global sparse synchronization. However, for sufficiently large $J_{\rm inter}$, due to strong inhibition the intermodular coupling strength plays a destructive role to spoil the pacing between sparse spikes. Hence, as $J_{\rm inter}$ passes a higher critical value $J_{{\rm inter},h}^*$ ($\simeq$1657) the global sparse synchronization breaks into unsynchronization. As an example, refer to the case of $J_{\rm inter} = 2500$. Sparse spikes in the raster plot of each subnetwork are completely scattered without forming any stripes [see Fig. 3(c)]; hence, each ISPSR kernel estimate $R_s^{(I)}(t)$ becomes nearly stationary (i.e., every subnetwork exhibits an unsynchronized state), as shown in Figs. 3(f1)–3(f4). We now vary not only $J_{\rm inter}$ but also $M_{\rm syn}^{\rm (inter)}$, and investigate emergence of modular and global sparse synchronization in the whole $J_{\rm inter}$-$M_{\rm syn}^{\rm (inter)}$ plane by using the method explained in Sec. III F. Thus, we obtain the state diagram in Fig. 3(g). Modular sparse synchronization emerges for small $J_{\rm inter}$ or $M_{\rm syn}^{\rm (inter)}$ in the "L"-shaped gray region, while in the dark gray region global sparse synchronization appears. For large $J_{\rm inter}$ (>1572), unsynchronization occurs between the modular and the global synchronization. Changes in the population behaviors along routes I, II, and III in Fig. 3(g) are given in the following sections.

1. *Effect of the intermodular coupling strength on population synchronization along route I*

In order to study the effect of the intermodular coupling $J_{\rm inter}$ on the population synchronization, we consider the case of route I with $M_{\rm syn}^{\rm (inter)} = 20$. Some results for this case are given for $J_{\rm inter} = 10$, 500, and 2500 in Figs. 3(a)–3(f4). As $J_{\rm inter}$ is increased, a transition from modular sparse synchronization to global sparse synchronization when passing a threshold $J_{\rm inter}^*$($\simeq$268) and eventually to unsynchronization when passing a higher threshold $J_{{\rm inter},h}^*$($\simeq$1657) occurs. The higher threshold $J_{{\rm inter},h}^*$ for the transition to unsynchronization is determined through calculation of the sub- and the whole-population order parameters $\langle \mathcal{O}_s^{(I)} \rangle_r$ and $\langle \mathcal{O}_w \rangle_r$ of Eqs. (13) and (14), where $\langle \cdots \rangle_r$ denotes an average over realizations. Figures 4(a1)–4(a4) show plots of $\langle \mathcal{O}_s^{(I)} \rangle_r$ and $\langle \mathcal{O}_w \rangle_r$ versus $J_{\rm inter}$. For $J_{\rm inter} < J_{{\rm inter},h}^*$ ($\simeq$1657), synchronized states exist because the values of $\langle \mathcal{O}_s^{(I)} \rangle_r$ and $\langle \mathcal{O}_w \rangle_r$ become saturated to nonzero limit values for large L. When passing the higher threshold threshold $J_{{\rm inter},h}^*$, a transition to unsynchronization occurs because the order parameters $\langle \mathcal{O}_s^{(I)} \rangle_r$ and $\langle \mathcal{O}_w \rangle_r$ tend to zero as $L \to \infty$. These unsynchronized states seem to appear due to a destructive effect of strong inhibition spoiling the pacing between sparse spikes. Here we present two explicit examples for the synchronized and the unsynchronized states. First, we consider the synchronized case for $J_{\rm inter} = 1600$. For $L = 10^3$, sparse stripes are formed in the raster plot of spikes for each subnetwork, and the ISPSR and the IWPSR kernel estimates $R_s^{(I)}(t)$ and $R_w(t)$ show regular oscillations, although there are some variations in the amplitudes [see Figs. 4(b) and 4(d)]. As L is increased to $L = 10^4$, stripes in the raster plots become more clear, and $R_s^{(I)}(t)$ and $R_w(t)$ display more regular oscillations with nearly the same amplitudes, as shown in Figs. 4(c) and 4(e). Consequently, the population state for $J_{\rm inter} = 1600$ seems to be synchronized because $R_s^{(I)}(t)$ and $R_w(t)$ tend to show more regular oscillations as L goes to the infinity. As a second example, we consider the unsynchronized case of $J_{\rm inter} = 1700$. As shown in Fig. 4(f) for $L = 10^3$, sparse spikes are scattered without forming any stripes in the raster plot, and $R_s^{(I)}(t)$ and $R_w(t)$ in Fig. 4(h) show little noisy fluctuations. In contrast to the synchronized case, as L is increased to $L = 10^4$, sparse spikes become more scattered, and consequently $R_s^{(I)}(t)$ and $R_w(t)$ become nearly stationary, as shown in Figs. 4(g) and 4(i). Hence, the population state for $J_{\rm inter} = 1700$ seems to be unsynchronized because $R_s^{(I)}(t)$ and $R_w(t)$ tend to be nearly stationary as L increases to the infinity.

In order to further understand the above synchronization-unsynchronization transition, we investigate the effect of intermodular connection on the "microscopic" dynamical cross-correlations between neuronal pairs. As examples, we reconsider the same cases of $J_{\rm inter} = 1600$ and 1700 as in Fig. 4. Figure 5(a1) shows the plots of the spatial cross-correlation functions $C_l^{(I)}$ of Eq. (17) versus l for $L = 10^3$ in the case of $J_{\rm inter} = 1600$. These spatial correlation functions $C_l^{(I)}$ are nearly nonzero constant ($\simeq$0.04) in the whole range of l; hence, the correlation length η_I becomes $L/2$ (=500), covering all of the subnetworks (note that the maximal distance between neurons is $L/2$ because of the ring architecture on which neurons exist). Consequently, each subnetwork is composed of just one single synchronized block. For $L = 10^4$, the flatness of $C_l^{(I)}$ in Fig. 5(a2) also extends to the whole range ($l = L/2 = 5000$) of the Ith subnetwork; hence, the correlation length becomes $\eta_I = 5000$, which also covers the whole subnetwork. In this way, for $J_{\rm inter} = 1600$, due to a constructive role of $J_{\rm inter}$ favoring the pacing between sparse spikes, the correlation length η_I seems to cover the whole subnetwork, independently of L. For this case, the normalized correlation length $\tilde{\eta}_I$ ($=\frac{\eta_I}{L}$), representing the ratio of the correlation length η_I to the subnetwork size L (i.e., denoting the relative size of synchronized blocks when compared to the whole subnetwork size), has a nonzero limit value, 1/2, and consequently synchronization emerges in each subnetwork. In contrast, for $J_{\rm inter} = 1700$ the spatial cross-correlation functions $C_l^{(I)}$ are nearly zero, independently of L, as shown in Figs. 5(b1) and 5(b2). For this case, due to a destructive role of $J_{\rm inter}$ spoiling the pacing between sparse spikes, the correlation length η_I becomes nearly zero; hence, no synchronization occurs in each subnetwork.

We now investigate the type of synchronization through measurement of the matching degree between the

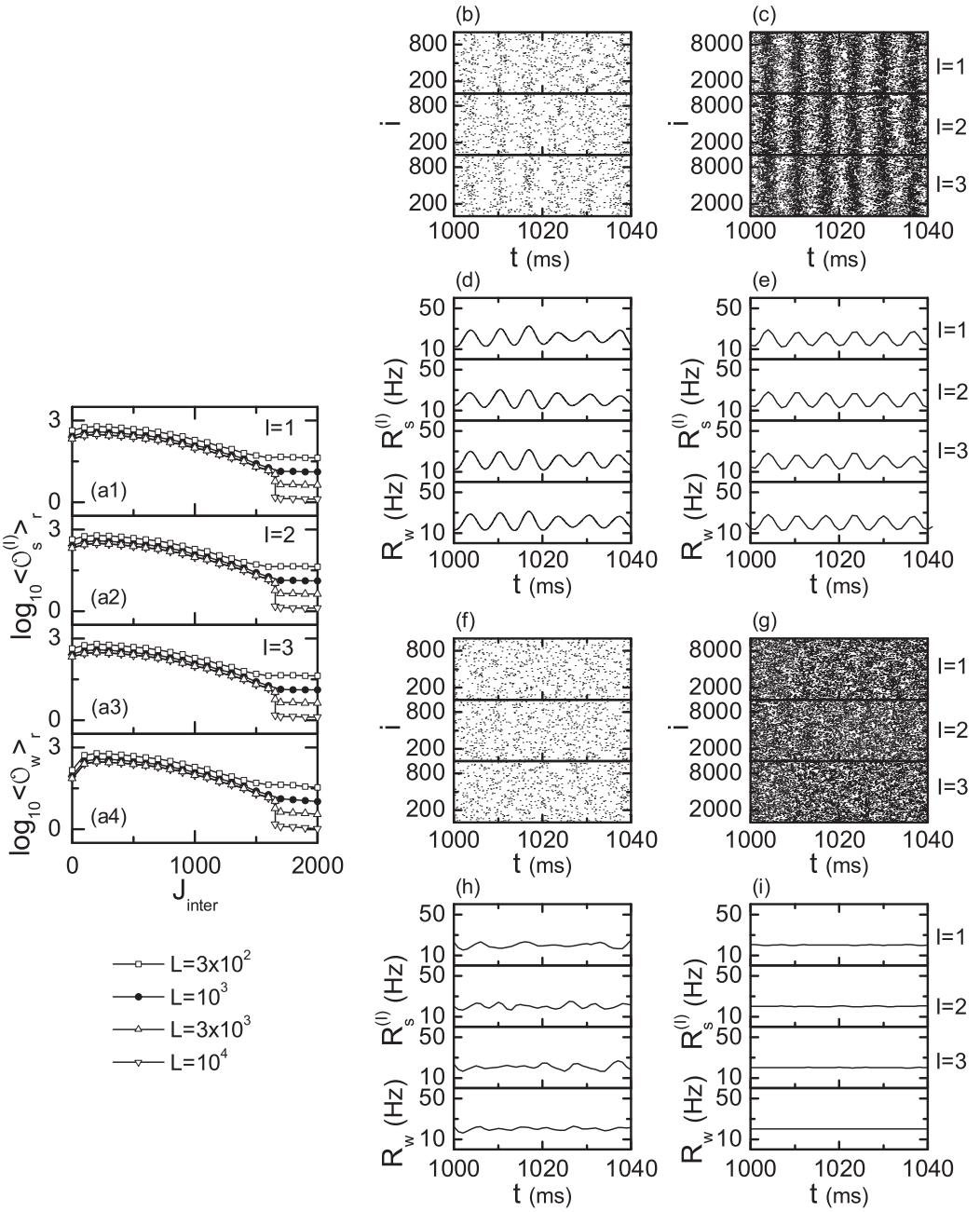

FIG. 4. Realistic thermodynamic order parameters for measurement of the threshold for the synchronization-unsynchronization transition along route I with $M_{\rm syn}^{\rm (inter)} = 20$ for the first case of intramodular dynamics with $p_{\rm rewiring} = 0.25$. (a1)–(a4) Plots of the sub- and the whole-population order parameters $\log_{10} \mathcal{O}_s^{(I)}$ ($I = 1,2,3$) and $\log_{10} \mathcal{O}_w$ versus $J_{\rm inter}$. Sparse synchronization for $J_{\rm inter} = 1600$: raster plots of neural spikes in the three subnetworks for (b) $L = 10^3$ and (c) $L = 10^4$ and instantaneous sub- and whole-population spike rate kernel estimates $R_s^{(I)}(t)$ ($I = 1,2,3$) and $R_w(t)$ for (d) $L = 10^3$ and (e) $L = 10^4$. Unsynchronization for $J_{\rm inter} = 1700$: raster plots of neural spikes in the three subnetworks for (f) $L = 10^3$ and (g) $L = 10^4$ and instantaneous sub- and whole-population spike rate kernel estimates $R_s^{(I)}(t)$ ($I = 1,2,3$) and $R_w(t)$ for (h) $L = 10^3$ and (i) $L = 10^4$.

intramodular dynamics in subnetworks in the synchronized range of $0 < J_{\rm inter} < J_{{\rm inter},h}^{*} (\simeq 1657)$ along route I in Fig. 3(g). Figures 6(a1)–6(a5) show the raster plots of spikes in the three subnetworks for $J_{\rm inter} = 10$, 30, 70, 400, and 1200, respectively. The ISPSR and the IWPSR kernel estimates, $R_s^{(I)}(t)$ and $R_w(t)$, for $J_{\rm inter} = 10$, 30, 70, 400, and 1200 are also shown in Figs. 6(b1)–6(b5), respectively. For each Ith subpopulation, sparse stripes are formed in the raster plot of spikes and the ISPSR kernel estimate $R_s^{(I)}(t)$ shows a regular oscillation with global frequency $f_p^{(I)} \simeq 147$ Hz. Hence, each subpopulation shows sparse synchronization. For the case of modular sparse synchronization for $J_{\rm inter} = 10$, 30, and 70, the intramodular dynamics of subnetworks make some mismatching because both the stripes and the ISPSR kernel estimates between the subnetworks are shifted [see Figs. 6(b1)–6(b3) where the minima of $R_s^{(I)}(t)$ (denoted by solid circles) lie off the reference vertical lines which pass the minima of $R_w(t)$ (represented by open circles)]. Hence,

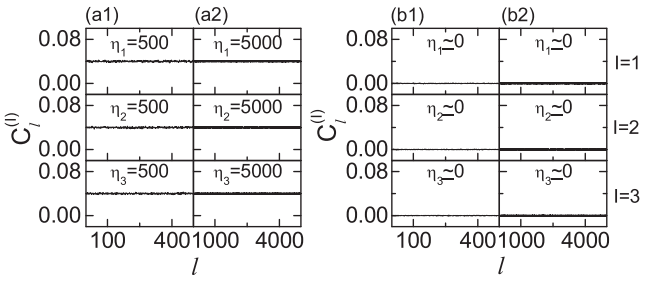

FIG. 5. Spatial cross-correlation functions for the synchronized and the unsynchronized states along route I with $M_{\rm syn}^{\rm (inter)} = 20$ for the first case of intramodular dynamics with $p_{\rm rewiring} = 0.25$. Sparse synchronization for $J_{\rm inter} = 1600$ with the spatial correlation length η_I covering the whole subnetwork: spatial cross-correlation functions $C_l^{(I)}$ in the three subnetworks ($I = 1,2,3$) for (a1) $L = 10^3$ and (a2) $L = 10^4$. Unsynchronization for $J_{\rm inter} = 1700$ with $\eta_I \simeq 0$: spatial cross-correlation functions $C_l^{(I)}$ in the three subnetworks for (b1) $L = 10^3$ and (b2) $L = 10^4$.

the amplitude of $R_w(t)$ becomes less than that of $R_s^{(I)}(t)$. As $J_{\rm inter}$ is increased, the mismatching degree decreases; hence, the amplitude of $R_w(t)$ increases. Eventually, when passing a threshold $J_{\rm inter}^*$ ($\simeq$268) global sparse synchronization occurs. Hence, for $J_{\rm inter} = 400$ and 1200, intramodular dynamics of subnetworks (shown in their raster plots and ISPSR kernel estimates) make perfect matching [i.e., the minima of $R_s^{(I)}(t)$ lie on the reference vertical lines, as shown in Figs. 6(b4) and 6(b5)]; hence, the amplitude of $R_w(t)$ becomes the same as that of $R_s^{(I)}(t)$. The matching degree between the intramodular dynamics of subnetworks may be measured through calculation of the cross-correlation modularity measure C_M of Eq. (19). Figure 6(d) shows the plot of $\langle C_M \rangle_r$ versus $J_{\rm inter}$ where $\langle \cdots \rangle_r$ denotes average over realizations. As $J_{\rm inter}$ is increased, $\langle C_M \rangle_r$ increases monotonically, and eventually, when passing the threshold $J_{\rm inter}^*$ ($\simeq$268), its value becomes 1. Hence, for $J_{\rm inter} < J_{\rm inter}^*$ modular sparse synchronization (with $\langle C_M \rangle_r < 1$) emerges, while global sparse synchronization (with $\langle C_M \rangle_r = 1$) appears for $J_{\rm inter}^* < J_{\rm inter} < J_{{\rm inter},h}^*$.

We also measure the degree of modular and global sparse synchronization in the synchronized range of $0 < J_{\rm inter} < J_{{\rm inter},h}^*$. As shown in Figs. 6(a1)–6(a5), spike synchronization may be well visualized in the raster plots of spikes. For a synchronous case, "stripes" (composed of spikes and representing population synchronization) appear successively in the raster plot. For measurement of the degree the sub- and the whole-population spike synchronization seen in the raster plots, realistic statistical-mechanical sub- and whole-population measures $M_s^{(I)}$ and $M_s^{(w)}$ are introduced by considering the occupation pattern (representing the density of the stripes) and the pacing pattern (denoting the smearing of the stripes) of spikes in the stripes for the sub- and the whole-populations, as explained in Sec. III G. By varying $J_{\rm inter}$, we follow 3×10^3 stripes (i.e., 3×10^3 global cycles) in each realization, and through an average over 20 realizations we obtain the sub- and the whole-population occupation degrees $\langle O_s^{(I)} \rangle_r$ and $\langle O_w \rangle_r$ of Eq. (21), the sub- and the whole-population pacing degrees $\langle P_s^{(I)} \rangle_r$ and $\langle P_w \rangle_r$ of Eq. (26), and the statistical-mechanical sub- and whole-population spiking measures $M_s^{(I)}$ and $M_s^{(w)}$ of Eq. (27), and the results are shown in Figs. 7(a1)–7(c4). For the case of modular synchronization [occurring on the left region of the vertical dotted threshold line for $J_{\rm inter} = J_{\rm inter}^*$ ($\simeq$268)], both the occupation degree $\langle O_w \rangle_r$ and the pacing degree $\langle P_w \rangle_r$ for the whole-population are less than those for the subpopulations because of mismatching between the intramodular dynamics of subnetworks. As $J_{\rm inter}$ is increased, their mismatching degrees become smaller, and eventually $\langle O_w \rangle_r$ and $\langle P_w \rangle_r$ for the whole population become the same as those for the subpopulations for the case of global synchronization (occurring on the right region of the vertical dotted threshold line) due to perfect matching between the intramodular dynamics of subnetworks. We first consider the occupation degree which characterizes the sparseness degree of population synchronization. For the subpopulations, the occupation degrees $\langle O_s^{(I)} \rangle_r$ decrease monotonically because of increase in inhibition with increasing $J_{\rm inter}$. In the case of modular synchronization, typical IWPSR kernel estimates $R_w(t)$ show faster and smaller-amplitude oscillations with the whole-population frequency $f_p^{(w)}$ larger than the subpopulation frequency $f_p^{(I)}$; hence, the occupation degree $\langle O_w \rangle_r$ for the whole-population becomes less than $\langle O_s^{(I)} \rangle_r$. As $J_{\rm inter}$ is increased, $\langle O_w \rangle_r$ increases and approaches $\langle O_s^{(I)} \rangle_r$ due to decrease in the mismatching degree between the intramodular dynamics of subnetworks, and eventually when passing the threshold $J_{\rm inter}^*$ (i.e., in the case of global synchronization) they become the same and then decrease with increasing $J_{\rm inter}$. We note that modular and global synchronization is sparse one because $\langle O_s^{(I)} \rangle_r$ is much less than unity [i.e., only a small fraction of the total L ($=10^3$) neurons in the subpopulation fire in each stripe]. Next we consider the pacing degree between spikes in the stripes. For relatively small $J_{\rm inter}$, with increasing $J_{\rm inter}$ the subpopulation pacing degree $\langle P_s^{(I)} \rangle_r$ increases due to a constructive role of $J_{\rm inter}$ favoring the pacing between spikes, while for large $J_{\rm inter}$ $\langle P_s^{(I)} \rangle_r$ decreases as $J_{\rm inter}$ is increased because of a destructive role of $J_{\rm inter}$ spoiling the pacing between spikes. Through competition between these constructive and destructive roles of $J_{\rm inter}$ a "plateau" with high pacing degree is formed in a relatively wide region of intermediate $J_{\rm inter}$ for the case of global sparse synchronization. The whole-population pacing degree $\langle P_w \rangle_r$ (which is less than or equal to $\langle P_s^{(I)} \rangle_r$) also exhibits similar behavior. Consequently, both the sub- and the whole-population statistical-mechanical spiking measures $M_s^{(I)}$ and $M_s^{(w)}$ (which are obtained by taking into consideration both the occupation and the pacing degrees of spikes in the stripes) show bell-shaped curves with their peaks at $J_{\rm inter} \simeq 202$ (corresponding to modular sparse synchronization) and $J_{\rm inter} \simeq 287$ (corresponding to global sparse synchronization), respectively. For further understanding of the pacing degree between spikes, we also consider the spatial cross correlations between neuronal pairs. Figures 7(d1)–7(d5) show the spatial cross-correlation functions $C_l^{(I)}$ of Eq. (17) for $J_{\rm inter} = 10$, 30, 70, 400, and 1200, respectively. For the case of relatively small $J_{\rm inter}$, with increasing $J_{\rm inter}$ the value of $C_l^{(I)}$ increases, but it decreases for large $J_{\rm inter}$. For quantitative analysis, we introduce the subpopulation spatial cross-correlation degree $\langle \langle C_l^{(I)} \rangle_l \rangle_r$ given by double averaging of the spatial cross-correlation function $C_l^{(I)}$ over all lengths l and realizations. This subpopulation spatial cross-correlation degree $\langle \langle C_l^{(I)} \rangle_l \rangle_r$

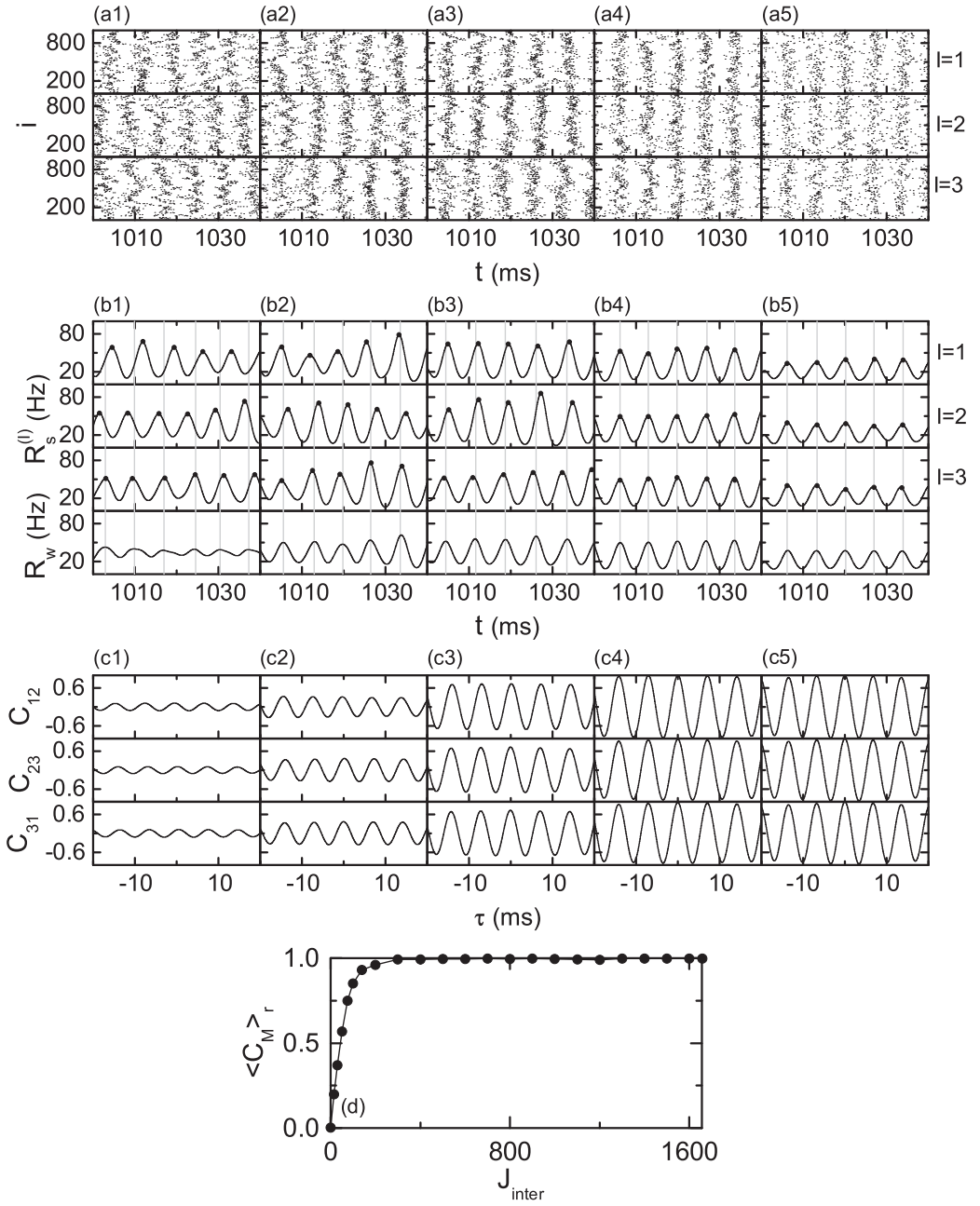

FIG. 6. Realistic cross-correlation modularity measure for determining the threshold for modular-global sparse synchronization transition along route I with $M_{syn}^{(inter)} = 20$ for the first case of intramodular dynamics with $p_{rewiring} = 0.25$. Raster plots of neural spikes in the subnetworks ($I = 1,2,3$) for $J_{inter} =$ (a1) 10, (a2) 30, (a3) 70, (a4) 400, and (a5) 1200. Instantaneous sub- and whole-population spike rate kernel estimates $R_s^{(I)}$ ($I = 1,2,3$) and $R_w(t)$ for $J_{inter} =$ (b1) 10, (b2) 30, (b3) 70, (b4) 400, and (b5) 1200. Vertical gray lines pass minima of $R_w(t)$, and the minima of $R_s^{(I)}(t)$ [$R_w(t)$] are represented by solid (open) circles. Temporal cross-correlation functions $C_{I,J}(\tau)$ between the ISPSR kernel estimates $R_s^{(I)}(t)$ and $R_s^{(J)}(t)$ of the subnetworks I and J for $J_{inter} =$ (c1) 10, (c2) 30, (c3) 70, (c4) 400, and (c5) 1200. (d) Plot of the cross-correlation modularity measure $\langle C_M \rangle_r$ versus J_{inter}.

is a microscopic measure quantifying the cross-correlation degree between the microscopic IISR kernel estimates $r_i^{(I)}(t)$ without any explicit relation to the macroscopic occupation and pacing patterns of spikes. Figure 7(e) shows plots of $\langle\langle C_l^{(I)}\rangle_l\rangle_r$ (obtained through averaging over 20 realizations) versus J_{inter} for $I = 1$, 2, and 3. Similar to the case of the subpopulation pacing degree $\langle P_s^{(I)}\rangle_r$, $\langle\langle C_l^{(I)}\rangle_l\rangle_r$ also display similar bell-shaped curves with peaks in the region of global synchronization. Hence, the statistical-mechanical pacing degree between spikes seems to be somewhat associated with the microscopic spatial cross-correlation degree between neuronal pairs.

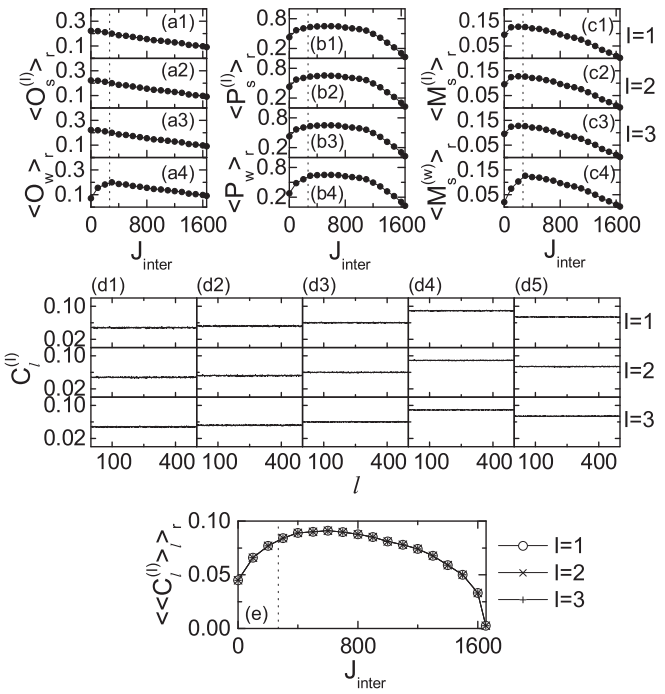

FIG. 7. Realistic statistical-mechanical spiking measure for measurement of the degree of modular and global sparse synchronization along route I with $M_{\rm syn}^{\rm (inter)} = 20$ for the first case of intramodular dynamics with $p_{\rm rewiring} = 0.25$. Vertical dotted lines in (a1)–(c4) and (e) represent the threshold of $J = J_{\rm inter}^{*}$ ($\simeq$268). (a1)–(a4) Plots of the sub- and the whole-population occupation degrees $\langle O_s^{(I)}\rangle_r$ and $\langle O_w\rangle_r$ versus $J_{\rm inter}$. (b1)–(b4) Plots of the sub- and the whole-population pacing degrees $\langle P_s^{(I)}\rangle_r$ and $\langle P_w\rangle_r$ versus $J_{\rm inter}$. (c1)–(c4) Plots of the sub- and the whole-population statistical-mechanical spiking measures $\langle M_s^{(I)}\rangle_r$ and $\langle M_s^{(w)}\rangle_r$ versus $J_{\rm inter}$. Spatial cross-correlation functions $C_l^{(I)}$ in the three subnetworks for $J_{\rm inter}$ = (d1) 10, (d2) 30, (d3) 70, (d4) 400, and (d5) 1200. (e) Plot of the spatial cross-correlation degree $\langle\langle C_l^{(I)}\rangle_l\rangle_r$ versus $J_{\rm inter}$.

2. *Effect of the average number of intermodular connections along routes II and III*

In addition to the above study on the effect of $J_{\rm inter}$ along route I for $M_{\rm syn}^{\rm (inter)} = 20$, we also investigate the effect of average number of intermodular connections per interneuron $M_{\rm syn}^{\rm (inter)}$ on emergence of modular and global sparse synchronization along routes II and III for $J_{\rm inter} = 500$ and 2500, respectively [see Fig. 3(g)]. For the case of route II with $J_{\rm inter} = 500$, the raster plots of spikes in the three subpopulations for $M_{\rm syn}^{\rm (inter)} = 2$, 5, 20, and 50 are shown in Figs. 8(a1)–8(a4), respectively. The corresponding ISPSR and IWPSR kernel estimates, $R_s^{(I)}(t)$ and $R_w(t)$, for $M_{\rm syn}^{\rm (inter)} = 2$, 5, 20, and 50 are also shown in Figs. 8(b1)–8(b4), respectively. For each Ith subpopulation, sparse stripes are formed in the raster plot and the ISPSR kernel estimate $R_s^{(I)}(t)$ shows a regular oscillation. As $M_{\rm syn}^{\rm (inter)}$ is increased, more clear stripes appear in the raster plots of subnetworks; hence, the amplitudes of $R_s^{(I)}(t)$ increase. Furthermore, with increasing $M_{\rm syn}^{\rm (inter)}$, the mismatching degree between the intramodular dynamics of subnetworks decreases, and eventually when passing a threshold $M_{\rm syn}^{\rm (inter)*}$ ($\simeq$9) perfect matching occurs. Figure 8(c) shows the plot of the cross-correlation modularity measure $\langle C_M\rangle_r$ of Eq. (19) versus $M_{\rm syn}^{\rm (inter)}$. Thus, for $M_{\rm syn}^{\rm (inter)} < M_{\rm syn}^{\rm (inter)*}$ modular sparse synchronization with $\langle C_M\rangle_r < 1$ emerges, while global sparse synchronization with $\langle C_M\rangle_r = 1$ appears for $M_{\rm syn}^{\rm (inter)} > M_{\rm syn}^{\rm (inter)*}$. In this way, with increasing $M_{\rm syn}^{\rm (inter)}$ the pacing degree between spikes increases monotonically, thanks to the increase in the degree of effectiveness of global communication between spikes. Hence, $M_{\rm syn}^{\rm (inter)}$ plays only a constructive role to favor the pacing between spikes in subnetworks as well as the matching between the intramodular dynamics of the subnetworks, in contrast to dual roles of $J_{\rm inter}$ for the case of route I. Hence, unsynchronization does not appear. This constructive role of $M_{\rm syn}^{\rm (inter)}$ may be seen explicitly in Figs. 8(d1) and 8(f2). We first consider the occupation degree which characterizes the sparseness degree of spike synchronization. For the case of modular synchronization, the subpopulation occupation degree $\langle O_s^{(I)}\rangle_r$ in the subnetworks decreases a little with increasing $M_{\rm syn}^{\rm (inter)}$, while $\langle O_s^{(I)}\rangle_r$ remains nearly constant for the case of global synchronization. On the other hand, as $M_{\rm syn}^{\rm (inter)}$ is increased the whole-population occupation degree $\langle O_w\rangle_r$ increases and approaches $\langle O_s^{(I)}\rangle_r$ because of the decrease in the mismatching degree between the intramodular dynamics of the subnetworks, and eventually when passing the threshold $M_{\rm syn}^{\rm (inter)*}$ they become the same and then remain nearly constant with increasing $M_{\rm syn}^{\rm (inter)}$. Hence, the constant behavior of $\langle O_s^{(I)}\rangle_r$ and $\langle O_w\rangle_r$ for the case of global synchronization (which may occur because the average inhibition given to each neuron is the same for constant intermodular coupling strength, independently of $M_{\rm syn}^{\rm (inter)}$) is in contrast to the monotonically decreasing behavior of $\langle O_s^{(I)}\rangle_r$ and $\langle O_w\rangle_r$ for the case of route I [refer to Figs. 7(a1)–7(a4)]. Since $\langle O_s^{(I)}\rangle_r < 1$ [i.e., only a small fraction of the total $L(=10^3)$ neurons in the subpopulation fire in each stripe], modular and global synchronization is sparse. Next we consider the pacing degree between spikes in the stripes. For both cases of modular and global sparse synchronization, with increasing $M_{\rm syn}^{\rm (inter)}$ both the sub- and the whole-population pacing degrees $\langle P_s^{(I)}\rangle_r$ and $\langle P_w\rangle_r$ increase monotonically due to a constructive role of $M_{\rm syn}^{\rm (inter)}$ favoring the pacing between the spikes, in contrast to the bell-shaped behavior for the case of route I [refer to Figs. 7(b1)–7(b4)]. Consequently, both the sub- and the whole-population statistical-mechanical spiking measures $M_s^{(I)}$ and $M_s^{(w)}$ (which are given by the products of the sub- and the whole-population occupation and pacing degrees) increase monotonically in both cases of modular and global sparse synchronization, which is also in contrast to the case of route I [refer to Figs. 7(c1)–7(c4)]. To further understand the pacing degree between spikes in the stripes, we consider the subpopulation spatial cross-correlation degree $\langle\langle C_l^{(I)}\rangle_l\rangle_r$ between neuronal pairs [given by double averaging of the spatial cross-correlation function $C_l^{(I)}$ of Eq. (17) over all lengths l and realizations]. Figure 8(g) shows plots of $\langle\langle C_l^{(I)}\rangle_l\rangle_r$ (obtained via average over 20 realizations) versus $M_{\rm syn}^{\rm (inter)}$ for $I = 1$, 2, and 3. Similar to the case of the subpopulation pacing degree $\langle P_s^{(I)}\rangle_r$, $\langle\langle C_l^{(I)}\rangle_l\rangle_r$ also displays monotonic increasing behavior. Hence, the statistical-mechanical pacing degree between spikes seems to be associated with the microscopic spatial cross-correlation degree between neuronal pairs, like the case of route I.

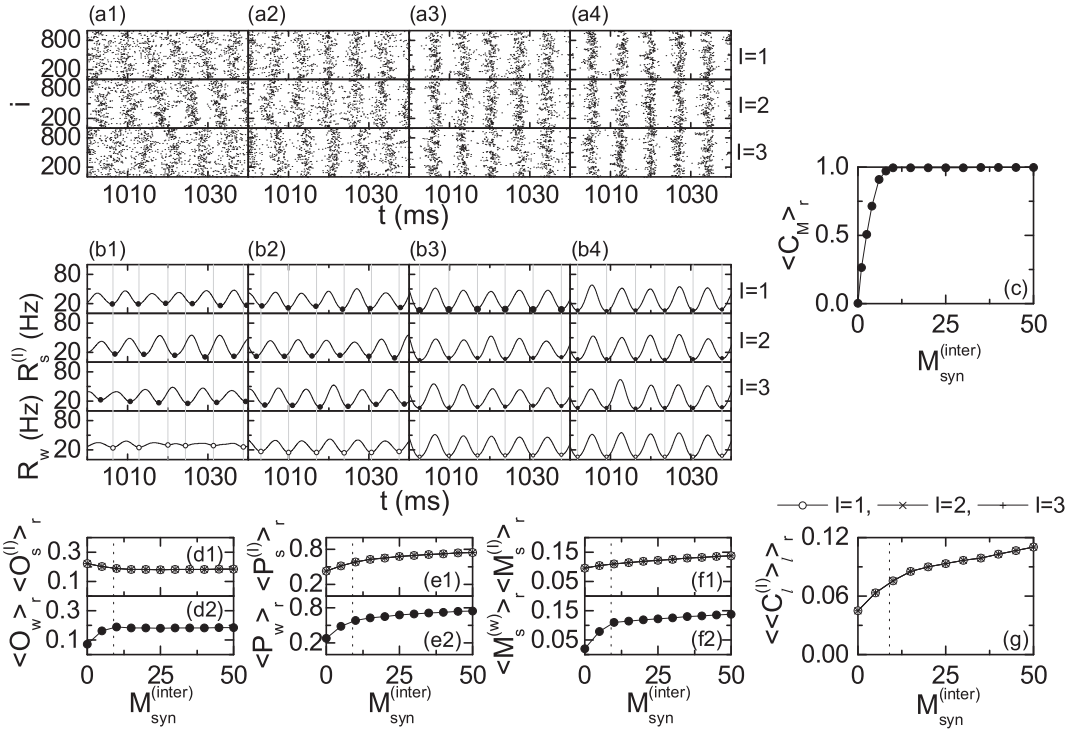

FIG. 8. Modular and global sparse synchronization along route II with $J_{\text{inter}} = 500$ for the first case of intramodular dynamics with $p_{\text{rewiring}} = 0.25$. Raster plots of neural spikes in the subnetworks ($I = 1,2,3$) for $M_{\text{syn}}^{(\text{inter})} = 2$ (a1), 5 (a2), 20 (a3), and 50 (a4). Instantaneous sub- and whole-population spike rate kernel estimates $R_s^{(I)}(t)$ ($I = 1,2,3$) and $R_w(t)$ for $M_{\text{syn}}^{(\text{inter})} = 2$ (b1), 5 (b2), 20 (b3), and 50 (b4). Vertical gray lines pass minima of $R_w(t)$, and the minima of $R_s^{(I)}(t)$ [$R_w(t)$] are represented by solid (open) circles. (c) Plot of the cross-correlation modularity measure $\langle C_M \rangle_r$ versus $M_{\text{syn}}^{(\text{inter})}$. Vertical dotted lines in (d1)–(g) denote the threshold $M_{\text{syn}}^{(\text{inter})*}(\simeq 9)$. (d1),(d2) Plots of the sub- and whole-population occupation degrees $\langle O_s^{(I)} \rangle_r$ and $\langle O_w \rangle_r$ versus $M_{\text{syn}}^{(\text{inter})}$. (e1),(e2) Plots of the sub- and the whole-population pacing degrees $\langle P_s^{(I)} \rangle_r$ and $\langle P_w \rangle_r$ versus $M_{\text{syn}}^{(\text{inter})}$. (f1),(f2) Plots of the sub- and the whole-population statistical-mechanical spiking measures $\langle M_s^{(I)} \rangle_r$ and $\langle M_s^{(w)} \rangle_r$ versus $M_{\text{syn}}^{(\text{inter})}$. (g) Plot of the spatial cross-correlation degree $\langle \langle C_l^{(I)} \rangle_l \rangle_r$ versus $M_{\text{syn}}^{(\text{inter})}$.

We also investigate the emergence of modular and global sparse synchronization by increasing $M_{\text{syn}}^{(\text{inter})}$ along route III for $J_{\text{inter}} = 2500$ (which is much larger than that for the case of route II). Unlike the case of route II, for small $M_{\text{syn}}^{(\text{inter})}$ a destructive effect to decrease the pacing degree between spikes occurs due to strong inhibition for $J_{\text{inter}} = 2500$; hence, when passing a lower threshold $M_{\text{syn},l}^{(\text{inter})*}$ ($\simeq 6$) a transition from modular sparse synchronization to unsynchronization occurs. However, with further increase in $M_{\text{syn}}^{(\text{inter})}$ a constructive effect of $M_{\text{syn}}^{(\text{inter})}$ to favor the pacing between spikes and the matching between the intramodular dynamics of subnetworks overcomes the destructive effect of strong inhibition. Consequently, a transition to global sparse synchronization occurs when passing a higher threshold $M_{\text{syn},h}^{(\text{inter})*}$ ($\simeq 26$). These results are well shown in Figs. 9(a1)–9(h). The raster plots of spikes in the three subpopulations for $M_{\text{syn}}^{(\text{inter})} = 1$, 5, 20, 30, and 50 are shown in Figs. 9(a1)–9(a5), respectively. The corresponding ISPSR and IWPSR kernel estimates, $R_s^{(I)}(t)$ and $R_w(t)$, for $M_{\text{syn}}^{(\text{inter})} = 1$, 5, 20, 30, and 50 are also shown in Figs. 9(b1)–9(b5), respectively. For each Ith subpopulation, sparse stripes are formed in the raster plot and $R_s^{(I)}(t)$ shows a regular oscillation, except for the unsynchronized case of $M_{\text{syn}}^{(\text{inter})} = 20$, where spikes are scattered without forming stripes in the raster plot and $R_s^{(I)}(t)$ is nearly stationary. Figures 9(c1)–9(c4) show the sub- and the whole-population order parameters $\mathcal{O}_s^{(I)}$ and $\mathcal{O}_w$, which determine a threshold for the synchronization-unsynchronization transition. In the region of $M_{\text{syn},l}^{(\text{inter})*} < M_{\text{syn}}^{(\text{inter})} < M_{\text{syn},h}^{(\text{inter})*}$, both $\mathcal{O}_s^{(I)}$ and $\mathcal{O}_w$ tend to zero in the thermodynamic limit of $L \to \infty$; hence, unsynchronized states appear due to a destructive effect of strong inhibition. On the other hand, for $M_{\text{syn}}^{(\text{inter})} < M_{\text{syn},l}^{(\text{inter})*}$ or $M_{\text{syn}}^{(\text{inter})} > M_{\text{syn},h}^{(\text{inter})*}$, the values of $\langle \mathcal{O}_s^{(I)} \rangle_r$ and $\langle \mathcal{O}_w \rangle_r$ become saturated to nonzero limit values for large L; hence, synchronized states exist. Particularly, for $M_{\text{syn}}^{(\text{inter})} > M_{\text{syn},h}^{(\text{inter})*}$ sparsely synchronized states appear due to a constructive effect of $M_{\text{syn}}^{(\text{inter})}$ favoring the pacing between spikes. The type of sparse synchronization may be determined in terms of the cross-correlation modularity measure C_M of Eq. (19), which is shown in Fig. 9(d). For $M_{\text{syn}}^{(\text{inter})} < M_{\text{syn},l}^{(\text{inter})*}$ modular sparse synchronization with $\langle C_M \rangle_r < 1$ (i.e., some mismatching between the intramodular dynamics of subnetworks) emerges, while global sparse synchronization with $\langle C_M \rangle_r = 1$ (i.e., perfect matching between the intramodular dynamics of subnetworks) appears for $M_{\text{syn}}^{(\text{inter})} > M_{\text{syn},h}^{(\text{inter})*}$. The degree of synchronization is also measured in terms of the occupation degrees, the pacing degrees, and the statistical-mechanical spiking measures in the sub- and the whole populations, which are shown in Figs. 9(e1)–9(g2). We first consider the case of modular sparse synchronization. As M_{syn} is increased, both the occupation

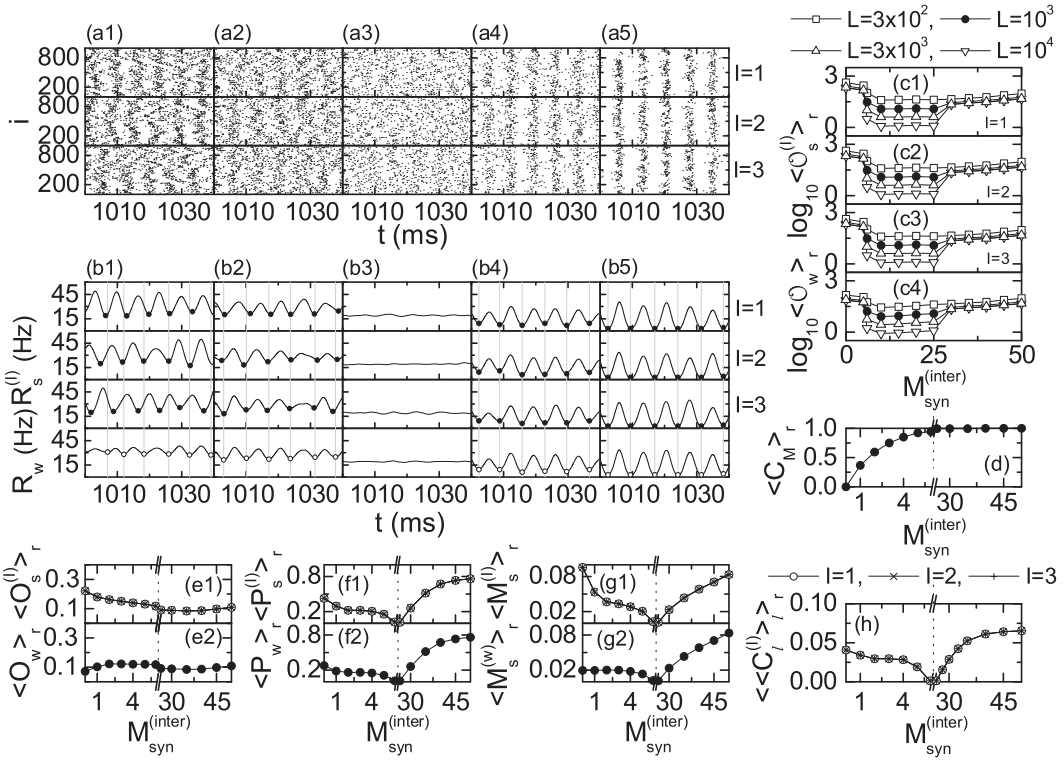

FIG. 9. Modular and global sparse synchronization along route III with $J_{\text{inter}} = 2500$ for the first case of intramodular dynamics with $p_{\text{rewiring}} = 0.25$. Raster plots of neural spikes in the subnetworks ($I = 1,2,3$) for $M_{\text{syn}}^{(\text{inter})} = 1$ (a1), 5 (a2), 20 (a3), 30 (a4), and 50 (a5). Instantaneous sub- and whole-population spike rate kernel estimates $R_s^{(I)}(t)$ ($I = 1,2,3$) and $R_w(t)$ for $M_{\text{syn}}^{(\text{inter})} = 1$ (b1), 5 (b2), 20 (b3), 30 (b4), and 50 (b5). Vertical gray lines pass minima of $R_w(t)$, and the minima of $R_s^{(I)}(t)$ [$R_w(t)$] are represented by solid (open) circles. (c1)–(c4) Plots of the sub- and the whole-population order parameters $\log_{10}\langle\mathcal{O}_s^{(I)}\rangle_r$ ($I = 1,2,3$) and $\log_{10}\langle\mathcal{O}_w\rangle_r$ versus $M_{\text{syn}}^{(\text{inter})}$. In (d)–(h), break symbols are given in the unsynchronization regions; the left (right) parts of the break symbols correspond to the regions of modular (global) synchronization. (d) Plot of the cross-correlation modularity measure $\langle C_M\rangle_r$ versus $M_{\text{syn}}^{(\text{inter})}$. (e1),(e2) Plots of the sub- and the whole-population occupation degrees $\langle O_s^{(I)}\rangle_r$ and $\langle O_w\rangle_r$ versus $M_{\text{syn}}^{(\text{inter})}$. (f1),(f2) Plots of the sub- and the whole-population pacing degrees $\langle P_s^{(I)}\rangle_r$ and $\langle P_w\rangle_r$ versus $M_{\text{syn}}^{(\text{inter})}$. (g1),(g2) Plots of the sub- and the whole-population statistical-mechanical spiking measures $\langle M_s^{(I)}\rangle_r$ and $\langle M_s^{(w)}\rangle_r$ versus $M_{\text{syn}}^{(\text{inter})}$. (h) Plot of the spatial cross-correlation degree $\langle\langle C_l^{(I)}\rangle_l\rangle_r$ versus $M_{\text{syn}}^{(\text{inter})}$.

degree $\langle O_s^{(I)}\rangle_r$ and the pacing degree $\langle P_s^{(I)}\rangle_r$ in the subnetworks decrease due to a destructive effect of strong inhibition for $J_{\text{inter}} = 2500$. In the whole population, with increasing M_{syn} the occupation degree $\langle O_w\rangle_r$ increases and approaches $\langle O_s^{(I)}\rangle_r$ because of decrease in the mismatching degree between the intramodular dynamics of subnetworks, and the pacing degree $\langle P_w\rangle_r$ decreases like the case of $\langle P_s^{(I)}\rangle_r$. Thus, both the sub- and the whole-population statistical-mechanical spiking measures $M_s^{(I)}$ and $M_s^{(w)}$ (which are given by the products of the sub- and the whole-population occupation and pacing degrees) decrease as $M_{\text{syn}}^{(\text{inter})}$ increases. On the other hand, for the case of global sparse synchronization, which is similar to the case of route II, the constructive effect of $M_{\text{syn}}^{(\text{inter})}$ favoring the pacing between spikes dominates. Consequently, with increasing $M_{\text{syn}}^{(\text{inter})}$ both $\langle P_s^{(I)}\rangle_r$ and $\langle P_w\rangle_r$ increase monotonically, while both $\langle O_s^{(I)}\rangle_r$ and $\langle O_w\rangle_r$ remain nearly constant because the average inhibition given to each neuron is the same for constant intermodular coupling strength J_{inter}, independently of $M_{\text{syn}}^{(\text{inter})}$. Consequently, as $M_{\text{syn}}^{(\text{inter})}$ is increased, the sub- and the whole-population statistical-mechanical spiking measures $M_s^{(I)}$ and $M_s^{(w)}$ show a monotonic increase. As in the case of route II, the modular and global synchronization is sparse because $\langle O_s^{(I)}\rangle_r$ is much less than unity. Furthermore, the statistical-mechanical pacing degree between spikes in the subpopulation seems to be associated with the spatial cross-correlation degree $\langle\langle C_l^{(I)}\rangle_l\rangle_r$ between neuronal pairs (obtained through averaging 20 realizations), which is shown in Fig. 9(h). For the case of modular sparse synchronization (i.e., $M_{\text{syn}}^{(\text{inter})} < M_{\text{syn},l}^{(\text{inter})*}$), with increasing $M_{\text{syn}}^{(\text{inter})}$ $\langle\langle C_l^{(I)}\rangle_l\rangle_r$ decreases monotonically due to a destructive role of strong inhibition, while for the case of global sparse synchronization (i.e., $M_{\text{syn}}^{(\text{inter})} > M_{\text{syn},h}^{(\text{inter})*}$), $\langle\langle C_l^{(I)}\rangle_l\rangle_r$ exhibits a monotonic increase because of a constructive role of $M_{\text{syn}}^{(\text{inter})}$.

B. Second and third cases of intramodular dynamics

To further examine the dependence of the intermodular connection effect on the type of intramodular dynamics, we consider the second and the third cases of the intramodular dynamics: (2) unsynchronized in the absence of intermodular coupling in all identical sub-networks with $p_{\text{rewiring}} = 0.05$ and (3) nonidentical subnetworks where, in the absence of intermodular coupling, the first subnetwork with $p_{\text{rewiring}} = 0.25$ is synchronized, the second subnetwork with

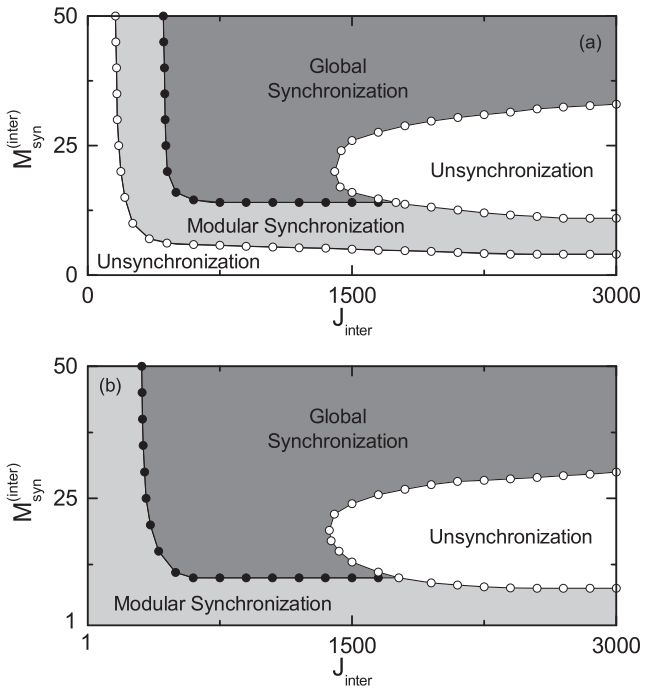

FIG. 10. (a) State diagram in the J_{inter}-$M_{\text{syn}}^{(\text{inter})}$ plane for the second case of the intramodular dynamics (i.e., in the absence of intermodular coupling, identically unsynchronized subnetworks with $p_{\text{rewiring}} = 0.05$). (b) State diagram in the J_{inter}-$M_{\text{syn}}^{(\text{inter})}$ plane for the third case of the intramodular dynamics (i.e., in the absence of intermodular coupling, synchronized in the first subnetwork with $p_{\text{rewiring}} = 0.25$, less synchronized in the second subnetwork with $p_{\text{rewiring}} = 0.15$, and unsynchronized in the third subnetwork $p_{\text{rewiring}} = 0.05$).

$p_{\text{rewiring}} = 0.15$ is also synchronized, but the third subnetwork with $p_{\text{rewiring}} = 0.05$ is unsynchronized. Figure 10(a) shows the state diagram in the J_{inter}-$M_{\text{syn}}^{(\text{inter})}$ plane for the second case of intramodular dynamics. This state diagram is similar to that for the first case in Fig. 3(g), except for the appearance of an "L"-shaped region of unsynchronization for small J_{inter} or $M_{\text{syn}}^{(\text{inter})}$. Beyond the unsynchronized region, modular and global sparse synchronization appears in the gray and the dark gray regions, respectively. For large J_{inter} (>1402) unsynchronization also occurs for large J_{inter} (>1402) between the modular and the global synchronizations. We also make an intensive investigation of emergence of modular and global sparse synchronization by changing J_{inter} along the route of $M_{\text{syn}}^{(\text{inter})} = 20$ (corresponding to the first route I for the first case). As in the first case, we obtain the raster plots of spikes in the three subpopulations and the corresponding ISPSR and IWPSR kernel estimates, $R_s^{(I)}(t)$ and $R_w(t)$ for representative values of $J_{\text{inter}} = 50$, 200, 600, 1000, and 2000; for brevity, associated figures are not presented. Unlike the first case 1 of the intramodular dynamics, for small J_{inter} ($=50$) unsynchronization occurs because of small p_{rewiring} ($=0.05$). For this case, the clustering coefficient is high; hence, partial stripes (indicating local clustering of spikes) seem to appear in the raster plots of spikes. Thus, the raster plots show zigzag patterns intermingled with partial stripes with diverse inclinations and widths; hence, spikes become difficult to keep pace with each other. Consequently, $R_s^{(I)}(t)$ and $R_w(t)$ become nearly stationary. However, as J_{inter} is increased and passes a lower threshold $J_{\text{inter},l}^*$ ($\simeq 187$), the intermodular coupling strength J_{inter} plays a constructive role to favor the pacing between spikes in each subnetwork, and synchronized states with regularly oscillating $R_s^{(I)}(t)$ and $R_w(t)$ appear for $J_{\text{inter}} = 200$, 600, and 1000. On the other hand, for large J_{inter}, due to strong inhibition, J_{inter} plays a destructive role to spoil the pacing between sparse spikes. Hence, when passing a higher threshold $J_{\text{inter},h}^*$ ($\simeq 1402$), a transition to unsynchronization occurs, as shown for $J_{\text{inter}} = 2000$. For this case, sparse spikes in the raster plots in each subnetwork are scattered without forming stripes; hence, both $R_s^{(I)}(t)$ and $R_w(t)$ become nearly stationary (i.e., every subnetwork exhibits an unsynchronized state). Similar to the first case, one can consider additional routes with fixed values of J_{inter} (e.g., 750 and 2300). As shown in the state diagram of Fig. 10(a), unsynchronization occurs for small $M_{\text{syn}}^{(\text{inter})}$, in contrast to the first case. However, when passing a threshold $M_{\text{syn}}^{(\text{inter})*}$ modular synchronization appears, and then the population behaviors are similar to those for the first case.

Finally, we consider the third case of nonidentical subnetworks where in the absence of intermodular coupling, the first subnetwork with $p_{\text{rewiring}} = 0.25$ is synchronized, the second subnetwork with $p_{\text{rewiring}} = 0.15$ is also synchronized, but the third subnetwork with $p_{\text{rewiring}} = 0.05$ is unsynchronized. Thanks to a constructive role of J_{inter} favoring the pacing between spikes, a transition to synchronization occurs in the third subnetwork when passing a lower threshold $J_{\text{inter},l}^*$. With increasing $M_{\text{syn}}^{(\text{inter})}$, the value of $J_{\text{inter},l}^*$ decreases due to a constructive effect of $M_{\text{syn}}^{(\text{inter})}$ to favor the pacing between spikes. For $J < J_{\text{inter},l}^*$, the third subnetwork is still unsynchronized, while the first and the second subsystems are synchronized. As J_{inter} passes $J_{\text{inter},l}^*$, the third subnetwork becomes synchronized, and then modular synchronization occurs due to mismatching between the intramodular dynamics of subnetworks. Here we consider the case of $J_{\text{inter}} > J_{\text{inter},l}^*$. Figure 10(b) shows the state diagram in the J_{inter}-$M_{\text{syn}}^{(\text{inter})}$ plane for the case of $J_{\text{inter}} \geqslant 1$ and $M_{\text{syn}}^{(\text{inter})} \geqslant 1$ (i.e., the region where the first and the second subnetworks are synchronized but the third subnetwork is unsynchronized is not shown). We note that this state diagram is nearly the same as that for the case 1 in Fig. 3(g). Modular sparse synchronization occurs in the "L"-shaped gray region, while global synchronization appears in the dark gray region. Unsynchronization also occurs for large J_{inter} (>1371) between modular and global synchronization. When compared with the first case of the intramodular dynamics, the regions of modular synchronization and unsynchronization are a little enlarged, while the region of global synchronization is somewhat contracted. We make an intensive study on appearance of modular and global synchronization by increasing J_{inter} from the threshold $J_{\text{inter},l}^*$($\simeq 0.2$) for the third subnetwork along the route of $M_{\text{syn}}^{(\text{inter})} = 20$ (corresponding to the first route I for the first case). Similar to the first case, we obtain the raster plots of spikes in the three subpopulations and the corresponding ISPSR and IWPSR kernel estimates, $R_s^{(I)}(t)$ and $R_w(t)$ for representative values of $J_{\text{inter}} = 10$, 100, 500, 1000, and 2000; for brevity, associated figures are not presented. For $J_{\text{inter}} = 10$, due to a constructive role of J_{inter} favoring the pacing between spikes, sparse stripes are formed in each Ith subpopulation ($I = 1,2,3$). However, in contrast to

case 1 of identical intramodular dynamics, the smearing degree of stripes is different, depending on the subpopulation. The stripes for the first subpopulation (with $p_{\rm rewiring} = 0.25$) are relatively clear, while the stripes in the other second and third subpopulations (with $p_{\rm rewiring} = 0.15$ and 0.05, respectively) are more and more smeared. Hence, the amplitudes of the regular oscillating $R_s^{(I)}(t)$ decrease as I is increased. As $J_{\rm inter}$ is further increased (e.g., $J_{\rm inter} = 100$ and 500), the pacing degree of spikes in the stripes increases for each subpopulation, although the stripes become more sparse. However, for large $J_{\rm inter}$ (e.g., $J_{\rm inter} = 1000$), due to a destructive role of $J_{\rm inter}$ the pacing degree of spikes in the stripes begins to decrease. Eventually, when passing a higher threshold $J^*_{{\rm inter},h}$ ($\simeq$1372) a transition to unsynchronization occurs. Thus, for $J_{\rm inter} = 2000$, spikes are scattered in the raster plot, and both $R_s^{(I)}(t)$ and $R_w(t)$ are nearly stationary. To study the effect of $M_{\rm syn}^{\rm (inter)}$, one may also consider other routes with fixed values of $J_{\rm inter}$ (e.g., 750 and 2300). With increasing $M_{\rm syn}^{\rm (inter)}$ along these routes, population behaviors are similar to those for the first case, as shown in the state diagram of Fig. 10(b).

V. SUMMARY

Sparsely interconnected modular structures are found in both mammalian brain anatomical networks and human brain functional networks, as in other complex systems such as social, technological, and biological networks. Modular organization of the brain network shows the anatomical substrate for segregation of the brain into specialized subregions with particular functional tasks. These specialized data of different features are also integrated to produce new useful information as a whole. In this way, the brain network is organized via the interplay between segregation (specialization) and integration (binding). We note that these real brains, composed of sparsely linked clusters, are far more complex than minimal nonclustered models such as small-world and scale-free networks. To take into consideration the modular structure of the real brain, we considered clustered small-world networks of inhibitory FS interneurons and investigated the effect of intermodular connection on emergence of sparsely synchronized rhythms at the sub- and whole-population levels by employing diverse realistic measures. By changing both the intermodular coupling strength $J_{\rm inter}$ and the average number of intermodular links per interneuron $M_{\rm syn}^{\rm (inter)}$, we made intensive study on the emergence of sparsely synchronized population states along the three routes in the $J_{\rm inter}$-$M_{\rm syn}^{\rm (inter)}$ plane for the first case of the intramodular dynamics: (1) synchronized in all identical subnetworks. Consequently, two kinds of sparse synchronization such as modular and global synchronization have been found to appear, in contrast to the case of nonclustered networks. Our main findings are that the type and degree of sparse synchronization depend on the intermodular parameters, $J_{\rm inter}$ and $M_{\rm syn}^{\rm (inter)}$. For lower values, $J_{\rm inter}$ acts to favor the pacing between spikes, while for higher values it tends to spoil the pacing between spikes due to strong inhibition. On the other hand, with increasing $M_{\rm syn}^{\rm (inter)}$ it acts to monotonically increase the pacing between spikes, which results from an increase in the degree of effectiveness of global communication between spikes. To examine the dependence on the intradynamics in the subnetworks, we have also considered two other cases for the intradynamics: (2) unsynchronized in all identical subnetworks and (3) synchronized and/or unsynchronized in nonidentical subnetworks. Figures 3(g), 10(a), and 10(b) show the state diagrams, representing main features on the population states, for the first, second, and third cases, respectively. For the second case, an "L"-shaped region of unsynchronization appears for small $J_{\rm inter}$ or $M_{\rm syn}^{\rm (inter)}$ because the intramodular dynamics in all subnetworks are unsynchronized in the absence of intermodular coupling. Beyond this "L"-shaped region, the structure of the state diagram is similar to that for the first case. In the third case, its state diagram is nearly the same as that for the first case. Due to nonidenticalness of subnetworks, modular synchronization persists a little more; hence, the region of modular synchronization is a little enlarged when compared to the first case. Moreover, in the case of modular synchronization the pacing degree of spikes varies depending on the subnetworks, in contrast to the first case of identical subnetworks. From the results in these three cases, it follows that the effect of intermodular connections seems to be essentially the same, independently of the type of intramodular dynamics in subnetworks. Finally, since changes in the coupling strengths and the synaptic connections are closely interwoven with the brain plasticity [86], we expect that our results on the intermodular connection effect in modular networks might have implications for the role of the brain plasticity in some functional behaviors related to population synchronization. However, explicit study on the interrelation among intermodular connection, population synchronization, and brain plasticity is beyond our present subject and it is left for future work.

ACKNOWLEDGMENTS

This research was supported by Basic Science Research Program through the National Research Foundation of Korea (NRF) funded by the Ministry of Education (Grant No. 2013057789).

[1] G. Buzsáki, *Rhythms of the Brain* (Oxford University Press, New York, 2006).

[2] R. D. Traub and M. A. Whittington, *Cortical Oscillations in Health and Diseases* (Oxford University Press, New York, 2010).

[3] X.-J. Wang, Physiol. Rev. **90**, 1195 (2010).

[4] E. H. Buhl, G. Tamas, and A. Fisahn, J. Physiol. **513**, 117 (1998).

[5] A. Fisahn, F. G. Pike, E. H. Buhl, and O. Paulsen, Nature (London) **394**, 186 (1998).

[6] J. Csicsvari, H. Hirase, A. Czurko, and G. Buzsáki, Neuron **21**, 179 (1998).

[7] J. Csicsvari, H. Hirase, A. Czurko, A. Mamiya, and G. Buzsáki, J. Neurosci. **19**, 274 (1999).
[8] J. Fellous and T. J. Sejnowski, Hippocampus **10**, 187 (2000).
[9] P. Fries, J. H. Reynolds, A. E. Rorie, and R. Desimone, Science **291**, 1560 (2001).
[10] N. K. Logothetis, J. Pauls, M. A. Augath, T. Trinath, and A. Oeltermann, Nature (London) **412**, 150 (2001).
[11] X.-J. Wang and G. Buzsáki, J. Neurosci. **16**, 6402 (1996).
[12] X.-J. Wang, in *Encyclopedia of Cognitive Science*, edited by L. Nadel (MacMillan, London, 2003), pp. 272–280.
[13] N. Brunel and V. Hakim, Neural Comput. **11**, 1621 (1999).
[14] N. Brunel, J. Comput. Neurosci. **8**, 183 (2000).
[15] N. Brunel and X.-J. Wang, J. Neurophysiol. **90**, 415 (2003).
[16] C. Geisler, N. Brunel, and X.-J. Wang, J. Neurophysiol. **94**, 4344 (2005).
[17] N. Brunel and D. Hansel, Neural Comput. **18**, 1066 (2006).
[18] N. Brunel and V. Hakim, Chaos **18**, 015113 (2008).
[19] W. Lim and S.-Y. Kim, J. Comput. Neurosci. **31**, 667 (2011).
[20] D.-G. Hong, S.-Y. Kim, and W. Lim, J. Korean Phys. Soc. **59**, 2840 (2011).
[21] S.-Y. Kim and W. Lim, J. Korean Phys. Soc. **63**, 104 (2013).
[22] O. Sporns, *Networks of the Brain* (MIT Press, Cambridge, UK, 2011).
[23] G. Buzsáki, C. Geisler, D. A. Henze, and X.-J. Wang, Trends Neurosci. **27**, 186 (2004).
[24] D. B. Chklovskii, B. W. Mel, and K. Svoboda, Nature (London) **431**, 782 (2004).
[25] S. Song, P. J. Sjöström, M. Reigl, S. Nelson, and D. B. Chklovskii, PLoS Biol. **3**, e68 (2005).
[26] O. Sporns and C. J. Honey, Proc. Natl. Acad. Sci. USA **103**, 19219 (2006).
[27] P. Larimer and B. W. Strowbridge, J. Neurosci. **28**, 12212 (2008).
[28] E. Bullmore and O. Sporns, Nat. Rev. Neurosci. **10**, 186 (2009).
[29] O. Sporns, G. Tononi, and G. M. Edelman, Cereb. Cortex **10**, 127 (2000).
[30] D. S. Bassett and E. Bullmore, Neuroscientist **12**, 512 (2006).
[31] D. Meunier, R. Lambiotte, and E. T. Bullmore, Front. Neurosci. **4**, 1 (2009).
[32] C. C. Hilgetag, G. A. P. C. Burns, M. A. O'Neill, J. W. Scannell, and M. P. Young, Philos. Trans. R. Soc. London B **355**, 91 (2000).
[33] C. C. Hilgetag and M. Kaiser, Neuroinformatics **2**, 353 (2004).
[34] O. Sporns, D. Chialvo, M. Kaiser, and C. Hilgetag, Trends Cognit. Sci. **8**, 418 (2004).
[35] S.-J. Wang, C. C. Hilgetag, and C. S. Zhou, Front. Comput. Neurosci. **5**, 30 (2011).
[36] D. A. Fair, A. L. Cohen, J. D. Power, N. U. F. Dosenbach, J. A. Church, F. M. Miezin, B. L. Schlaggar, and S. E. Petersen, PLoS Comput. Biol. **5**, e1000381 (2009).
[37] Y. He, J. Wang, L. Wang, Z. J. Chen, C. Yan, H. Yang, H. Tang, C. Zhu, Q. Gong, Y. Zang, and A. C. Evans, PLoS One **4**, e5226 (2009).
[38] D. Meunier, R. Lambiotte, A. Fortino, K. Ersche, and E. T. Bullmore, Front. Neuroinf. **3**, 37 (2009).
[39] L. Zemanová, C. S. Zhou, and J. Kurths, Physica D (Amsterdam, Neth.) **224**, 202 (2006).
[40] C. Zhou, L. Zemanová, G. Zamora, C. C. Hilgetag, and J. Kurths, Phys. Rev. Lett. **97**, 238103 (2006).
[41] C. Zhou, L. Zemanová, G. Zamora-López, C. Hilgetag, and J. Kurths, New J. Phys. **9**, 178 (2007).
[42] G. Zamora-López, C. Zhou, and J. Kurths, Chaos **19**, 015117 (2009).
[43] G. Zamora-López, C. Zhou, and J. Kurths, Front. Neuroinf. **4**, 1 (2010).
[44] G. Zamora-López, C. Zhou, and J. Kurths, Front. Neurosci. **5**, 83 (2011).
[45] O. Sporns, C. J. Honey, and R. Kötter, PLoS One **2**, e1049 (2007).
[46] P. Hagmann, L. Cammoun, X. Gigandet, R. Meuli, C. J. Honey, V. J. Wedeen, and O. Sporns, PLoS Biol. **6**, e159 (2008).
[47] D. J. Watts and S. H. Strogatz, Nature (London) **393**, 440 (1998).
[48] S. H. Strogatz, Nature (London) **410**, 268 (2001).
[49] D. J. Watts, *Small Worlds: The Dynamics of Networks Between Order and Randomness* (Princeton University Press, Princeton, NJ, 2003).
[50] S. Milgram, Psychol. Today **1**, 61 (1967).
[51] J. Guare, *Six Degrees of Separation: A Play* (Random House, New York, 1990).
[52] L. F. Lago-Fernández, R. Huerta, F. Corbacho, and J. A. Sigüenza, Phys. Rev. Lett. **84**, 2758 (2000).
[53] O. Kwon and H. T. Moon, Phys. Lett. A **298**, 319 (2002).
[54] A. Roxin, H. Riecke, and S. A. Solla, Phys. Rev. Lett. **92**, 198101 (2004).
[55] M. Kaiser and C. C. Hilgetag, PLoS Comput. Biol. **2**, e95 (2006).
[56] H. Riecke, A. Roxin, S. Madruga, and S. Solla, Chaos **17**, 026110 (2007).
[57] S. Achard and E. T. Bullmore, PLoS Comput. Biol. **3**, e17 (2007).
[58] S. Yu, D. Huang, W. Singer, and D. Nikolie, Cereb. Cortex **18**, 2891 (2008).
[59] Q. Wang, Z. Duan, M. Perc, and G. Chen, Europhys. Lett. **83**, 50008 (2008).
[60] M. Shanahan, Phys. Rev. E **78**, 041924 (2008).
[61] M. Ozer, M. Perc, and M. Uzuntarla, Phys. Lett. A **373**, 964 (2009).
[62] Q. Wang, M. Perc, Z. Duan, and G. Chen, Physica A (Amsterdam, Neth.) **389**, 3299 (2010).
[63] J. T. Lizier, S. Pritam, and M. Prokopenko, Artif. Life **17**, 293 (2011).
[64] S.-Y. Kim and W. Lim, Physica A (Amsterdam, Neth.) **421**, 109 (2015).
[65] X. Sun, J. Lai, M. Perc, J. Kurths, and G. Chen, Chaos **21**, 016110 (2011).
[66] C. A. S. Batista, E. L. Lameu, A. M. Batista, S. R. Lopes, T. Pereira, G. Zamora-López, J. Kurths, and R. L. Viana, Phys. Rev. E **86**, 016211 (2012).
[67] H.-T. Yu, J. Wang, B. Deng, and X.-L. Wei, Chin. Phys. B **22**, 018701 (2013).
[68] E. L. Lameu, C. A. S. Batista, A. M. Batista, K. Iarosz, R. L. Viana, S. R. Lopes, and J. Kurths, Chaos **22**, 043149 (2012).
[69] T. de L. Prado, S. R. Lopes, C. A. S. Batista, J. Kurths, and R. L. Viana, Phys. Rev. E **90**, 032818 (2014)
[70] S.-Y. Kim and W. Lim, Phys. Rev. E **92**, 022717 (2015).
[71] S.-Y. Kim and W. Lim, J. Neurosci. Methods **226**, 161 (2014).
[72] E. M. Izhikevich, IEEE Trans. Neural Networks **14**, 1569 (2003).
[73] E. M. Izhikevich, IEEE Trans. Neural Networks **15**, 1063 (2004).

[74] E. M. Izhikevich, *Dynamical Systems in Neuroscience* (MIT Press, Cambridge, UK, 2007).
[75] E. M. Izhikevich, Philos. Trans. R. Soc., A **368**, 5061 (2010).
[76] A. L. Hodgkin, J. Physiol. **107**, 165 (1948).
[77] E. M. Izhikevich, Int. J. Bifurcation Chaos Appl. Sci. Eng. **10**, 1171 (2000).
[78] M. San Miguel and R. Toral, in *Instabilities and Nonequilibrium Structures VI*, edited by J. Martinez, R. Tiemann, and E. Tirapegui (Kluwer Academic, Dordrecht, 2000), p. 35.
[79] H. Shimazaki and S. Shinomoto, J. Comput. Neurosci. **29**, 171 (2010).
[80] D. Hansel and G. Mato, Neural Comput. **15**, 1 (2003).
[81] D. Hansel and H. Sompolinsky, Phys. Rev. Lett. **68**, 718 (1992).
[82] I. Ginzburg and H. Sompolinsky, Phys. Rev. E **50**, 3171 (1994).
[83] D. Golomb and J. Rinzel, Physica D (Amsterdam, Neth.) **72**, 259 (1994).
[84] A. Longtin, Nuovo Cimento D **17**, 835 (1995).
[85] A. Longtin, in *Stochastic Dynamics and Pattern Formation in Biological and Complex Systems*, edited by S. Kim, K. J. Lee, and W. Sung (AIP, New York, 2000), pp. 219–239.
[86] A. Pascual-Leone, C. Freitas, L. Oberman, J. C. Horvath, M. Halko, M. Eldaief, S. Bashir, M. Vernet, M. Shafi, B. Westover, A. M. Vahabzadeh-Hagh, and A. Rotenberg, Brain Topogr. **24**, 302 (2011).